Spring 2011

Simulation of the field electron emission characteristics of a flat panel X-ray source

Chrystian Mauricio Posada Arbeláez

Follow this and additional works at: https://scholarsmine.mst.edu/masters_theses

Part of the Nuclear Engineering Commons

Department:

Recommended Citation

SIMULATION OF THE FIELD ELECTRON EMISSION

CHARACTERISTICS OF A FLAT PANEL X-RAY SOURCE

by

CHRYSTIAN MAURICIO POSADA ARBELAEZ

A THESIS

Presented to the Faculty of the Graduate School of the

MISSOURI UNIVERSITY OF SCIENCE AND TECHNOLOGY

In Partial Fulfillment of the Requirements of the Degree

MASTER OF SCIENCE IN NUCLEAR ENGINEERING

2011

Approved by

Carlos H. Castaño, Advisor
Gary E. Mueller
Shoaib Usman

ABSTRACT

A distributed flat panel x-ray source is designed as an alternative for medical and industrial imaging fields. The distributed x-ray source corresponds to a two dimensional array of micro (~100µm) x-ray cells similar in format to a field emission display. In this paper the electron field emission characteristics of a single of the proposed micro-sized x-ray cells are simulated. The field electron emission from the CNTs-based cathode is simulated using the Particle-In-Cell code OOPIC Pro. The electron source is simulated as a triode structure, composed of an emitting cathode, extracting grid and anode. The possibility of using focusing lenses to control the trajectory of emitted electrons is evaluated as well. The CNT emitters are modeled as pure Fowler-Nordheim emitters. The field emission characteristics were analyzed for extracting voltages between 25 V and 70 V and accelerating voltages between 30 kV and 120kV. Under these conditions, J_{FN}-V curves, energy distributions and electron distributions at the anode surface were determined. Electron trajectories were determined as well. When no focusing structures were employed, electron trajectories were found to be divergent. When focusing structures were included in the triode structure, the emitted electrons could be made to converge at the anode. In the focused cases, a dependency between the focal spot size and the extracting grid voltage was found. Results indicate an early feasibility of the proposed device to be employed as electron source in the proposed distributed flat panel x-ray source.

Keywords: Field Electron Emission, Cold Cathode, Flat Panel X-Ray Source, Particle-In-Cell (PIC), OOPIC Pro, Carbon Nanotubes (CNTs), Electron Source.

ACKNOWLEDGEMENTS

I would like to express my appreciation to those who made this thesis possible. I owe my deepest gratitude to my Advisor, Dr. Carlos H. Castaño. Since my arrival at Missouri University of Science and Technology two years ago – and even before then – he made his support available in a number of ways. Without his enthusiasm, inspiration, guidance and funding, it would have been impossible for me to write this acknowledgement page.

I would like to thank to Dr. Kumar, Dr. Usman and Dr. Mueller for all their support and instruction. Also, I would like to express my special gratitude to Dr. Lee for being a continuous source of ideas and inspiration for my research work.

I am indebted to my undergraduate professors at the National University of Colombia. They provided me with the basis necessary to successfully complete this stage of my career. I am especially grateful to Carlos I. Sanchez, Carlos M. García, Diego L. Durango, Hernán D. Álvarez and Veselina Pashova.

I wish to thank my student colleagues for providing a fun and stimulating environment in which to learn. I am especially grateful to Lucas Tucker, Edwin Grant, Hiral Patel and Zak Kulage. They have made the long hours in the office enjoyable and my transition to the United States easier.

My special thanks to all my friends for their support, company and collaboration. I wish to thank especially to Edward Anculle, Manuel Numpaque, Daniel Robledo and Natalia Pérez.

Lastly, and most importantly, I wish to thank my mom Miriam Arbeláez and my little brother Mateo Gómez Arbeláez. They are the greatest support I have in life and the biggest motivation for growing everyday as a person and as a professional.

TABLE OF CONTENTS

LIST OF ILLUSTRATIONS

LIST OF TABLES

1. INTRODUCTION

1.1. CONVENTIONAL X-RAY TUBES

X-rays were first discovered by Roentgen in 1895. With his discovery Roentgen opened the door to a new way to practice medicine; allowing doctors to view inside patients without physically open their bodies [1]. However, the mechanism behind the x-ray generation in the x-ray tubes has changed little since Roentgen first discovered them. The x-ray tubes being used today in medical or industrial applications are composed of a cathode and an anode encapsulated in a glass envelope as shown in Figure1.1 [1]. Electrons are thermionically emitted at the cathode, which is composed of one or several helical coil filaments made of a refractory material such as Mo or Mo-W alloys. During operation, filaments are kept at temperatures as high as 2200 °C and carry currents ranging between 3.5 and 5A [1]. Electrons emitted from the cathode are accelerated toward the anode, due to a high voltage (30 ~ 150 kV) applied across the cathode-anode gap. The anode is usually made of a thin target of tungsten or tungsten alloy [1]. A field shaping technique is used in order to focus the high energy electrons on a small region (0.1 to 1.5 mm^2) of the target. The small region where electrons strike the target is denominated *focal spot*. After the electrons strike the target, x-rays are generated by Bremsstrahlung interactions between target atoms and high energy incident electrons.
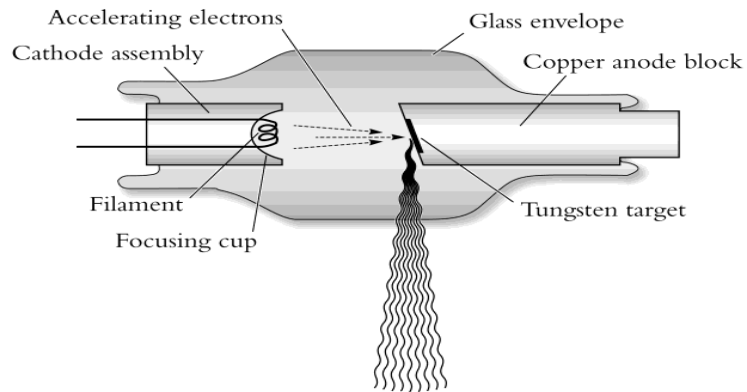
Figure 1.1. Schematic diagram of the conventional x-ray tube [1].

Today, these conventional x-ray tubes are the only choice available as a reliable source of x-rays for imaging purposes. However, the x-ray generation due to bremsstrahlung interactions is a very inefficient process. More than 99% of the total electron energy is converted into heat in the target, leading to x-ray generation efficiencies of less than 1% [1]. In consequence, heat accumulation in the target and operation of x-ray tubes are always limited by the ability to dissipate heat in the tube. Also, in conventional x-ray tubes x-ray photons generated from a single focal spot constitute a wide diverging beam. It causes geometric distortion of the patient anatomy or internal 3D structures of imaged objects due to magnification [1].

1.2. DISTRIBUTED FLAT PANEL X-RAY SOURCE

A solution to the problems of conventional x-ray tubes is the design and fabrication of a distributed flat panel x-ray source for medical and industrial x-ray imaging. The flat panel x-ray source is based on a two dimensional array of micro (50~100 μm) x-ray cells similar in format to conventional flat panel displays (see Figure 1.2).
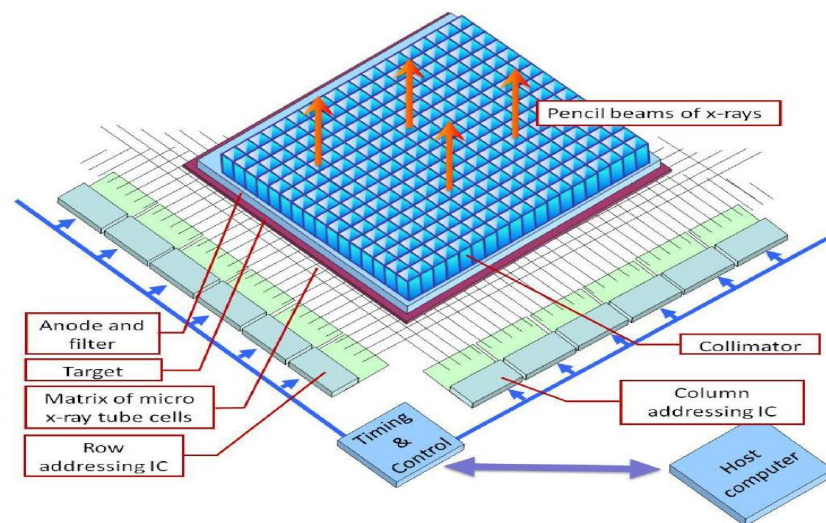
Figure 1.2. Schematic diagram of the distributed flat panel x-ray source.

In such x-ray source, x-ray generation in each of the micro cells can be controlled independently from the others. This characteristic allows the x-ray source to be operated in scanning mode, in which only one or a few cells produce x-rays at a time. Using this technique, scattered x-ray photons can be almost completely rejected, so that high quality, high contrast images can be produced. Also, the parallel x-ray beams generated in each micro x-ray source will reduce image distortion due to magnification, and the space required between the source and the image detector will be smaller.

In the proposed flat panel x-ray source, each micro cell is composed of a triode structure as shown in Figure 1.3. In this triode structure, electrons are field emitted from the cathode. A semitransparent metal micro mesh is used as extraction grid. In order to extract the electrons from the cathode, low voltage bias are applied between the cathode-grid gap. The emitted electrons are accelerated toward the anode due to high voltage bias applied between the cathode- anode gap. The high voltages used to accelerate the electrons toward the anode range between 30 ~ 150 kV. Transmission x-rays are generated at the anode by bremsstrahlung interactions between a thin x-ray target material and high energy electrons. As mentioned before, in this x-ray source, instead of using the conventional hot filament, electrons are extracted from a cold cathode using field emission mechanisms.
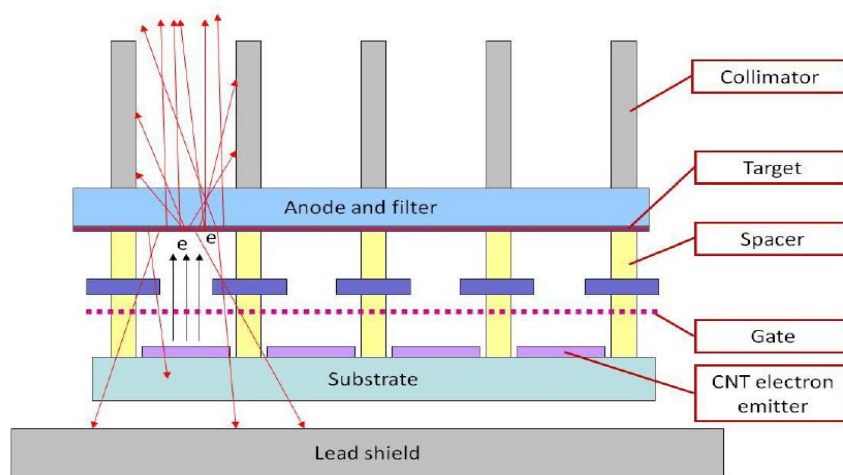
Figure 1.3. Cross sectional view of the proposed CNTs-based flat panel x-ray source.

Field emission is preferred over thermionic emission because no heating is required to extract the electrons and the emission of electrons can be controlled using an externally applied electric field [2-5]. These characteristics allow the field electron emission from each micro x-ray cell to be controlled individually, in a fast and accurate way, allowing the x-ray source to be operated in scanning mode if desired. When the x-ray source is operated in scanning mode, scattered x-rays can be almost completely rejected, so that high quality, high contrast images can be produced with low patient doses. In addition, when operating in scanning mode, the heat generated from a single cell can be dissipated over the whole anode structure, offering an alternative to the problem of heat accumulation in the x-ray target. These interesting features make a distributed x-ray source technically and scientifically attractive.

In order to fulfill these operational requirements, securing a reliable electron source is vital for the success of the flat panel x-ray project. Due to their high aspect ratio and low voltage threshold for field emission, carbon nanotubes have been preselected as potential field emitter materials for this project [4, 5]. In consequence, in this work an analysis of the field electron emission characteristics of the CNTs based triode structure proposed as source of electrons for each of the micro x-ray cells is presented.

The two dimensional Particle in Cell (PIC) code OOPIC Pro was used to simulate the emission of electrons from the CNT emitters. The field electron emission characteristics of the proposed triode structure were determined according to the results obtained from the simulations.

Results presented in this work include the evaluation of the trajectory of emitted electrons with and without focusing structures. Results also include the J_{FN}-V curves built for the system for extracting voltages between 25 and 70V and accelerating voltages between 30 and 120kV. Other results include the determination of a correlation between the accelerating voltage and the average energy of electrons striking the anode. The current density and energy distribution of electrons at the anode is included as well. Additionally, suggestions for future work that would improve the results obtained are presented.

2. BACKGROUND AND RATIONALE

2.1 ELECTRON FIELD EMISSION

Field emission (FE) refers to the process of extracting electrons from the surface of a material under the influence of an externally applied electric field. The mechanisms for the emission of electrons, as well as a potential energy diagram at the interface material-vacuum is presented in Figure 2.1 [3, 6]. As shown in Figure 2.1., electrons stay near the Fermi level at room temperature. In order to be emitted, electrons need to overcome a potential barrier given by the difference in height between the Fermi and vacuum levels, also known as work function of the material (Φ). The shape of this potential barrier is determined by image potential effects [6]. As shown in Figure 2.1, in the absence of an electric field, the potential barrier has infinite width and its height is given by the work function (Φ). In this case, for the emission of electrons to occur, electrons are required to jump over the top of the potential barrier. This mechanism is denominated *thermionic emission* and is the dominant mechanism for the emission of electrons from surfaces at high temperatures [2, 3, 6].
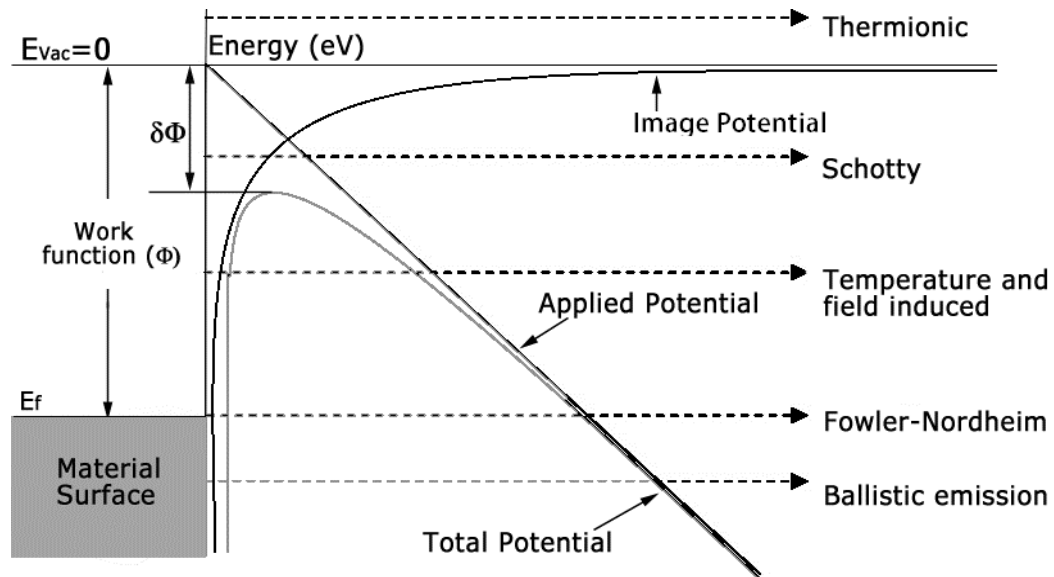
Figure 2.1 .Proposed mechanisms for emission of electrons from a solid material [3, 6].

On the other hand, if a strong electric field is applied, the potential barrier is deformed (Schottky effect), so that it becomes finite in width. These conditions allow electrons to quantum mechanically tunnel through the distorted potential barrier instead of having to jump over it. This mechanism for the emission of electrons is denominated *field emission* [2, 3, 6, 7]. The field emission (FE) mechanism was first explained by Fowler and Nordheim in 1928 [2]. It was established by Fowler and Nordheim that at low temperatures, the emission current of electrons from a material surface is a function of the work function (Φ) of the material, the applied electric field (E) and a field enhancement factor (β) due to special geometric configurations of the emitting material [2, 3].

The general form of the Fowler-Nordheim (F-N) equation is to:

$$J_{FN} = \frac{A_{FN}(\beta_{FN}E)^2}{\Phi_w} \exp\left(\frac{B_{FN}v(y)\Phi_w^{3/2}}{\beta_{FN}E}\right) \tag{1}$$

with,

$$A_{FN} = \frac{e^3 8\pi}{h_p} = 1.5415 \times 10^{-6} \, [A \, eV \, V^{-2}] \tag{2}$$

and

$$B_{FN} = -\frac{4}{3}\frac{(2m_e)^{1/2}}{e\,(h_p/2\pi)} = 6.8309 \times 10^9 \, [eV^{-3/2} \, V \, m^{-1}] \tag{3}$$

In this equation, J_{FN} is the emitted current density [mA/mm^2], E is the effective electric field acting over the emitting surface [V/m], β_{FN} is a field enhancement factor, Φ_w corresponds to the characteristic work function of the emitting material [eV], e and m_e are the charge and mass of the electron respectively and h_p is the Planck's constant. The other correction parameters can be found using the functional forms:

$$y = C_y E^{1/2}/\Phi_w \tag{4}$$

and,

$$v(y) = 1 - C_v y^2 \tag{5}$$

Where C_y and C_v are correction factors discussed somewhere else [35].

2.2 CARBON NANOTUBES AS FIELD EMITTERS

The synthesis of micro-sized filaments of graphite using an arc discharge method was first reported by Bacon et al. in the mid 50s [8]. However, it was only until 1991 when Iijima reported the synthesis of what he described as "helical microtubes of graphitic carbon" that carbon nanotubes (CNTs) gained the attention they have today [9]. Since Iijima reported the synthesis of CNTs with diameters between 4 and 30 nm and up to 1 μm length, the properties and diverse potential applications of CNTs have been extensively studied. Some of these applications include hydrogen storage materials [10], microelectronics [11], production and enhancement of composites materials [12], batteries, supercapacitors and sensors, [13, 14], etc. . However, due to their electronic and mechanical properties most of the research on CNTs has been focused on studying their excellent field emission characteristics [5, 15]. In fact, Baughman et al., published a review paper in 2002 summarizing the main areas of research involving CNTs [16]. In this review, the authors not only pointed out the fast growing interest on CNTs related research but they also reported the preferred areas of research on CNTs. Results indicated that most of the research initiatives involving CNTs had been concentrated on the evaluation of their synthesis and processing characteristics and their potential applications in field emission devices (see Figure 2.2).

The field emission characteristics of CNTs were first reported by W. de Heer et al., less than two decades ago [17].They evaluated the field emission characteristics of an array of carbon nanotubes based on the emitting capacity of graphite samples. Results obtained from their experiments indicated that it was possible to get emission current densities of up to 30μA/mm^2 at low voltages from a small array of CNTs. Since de Heer's discovery, the emission of electrons from CNTs has been extensively studied both for applications that range from flat panel displays to electron microscopes.
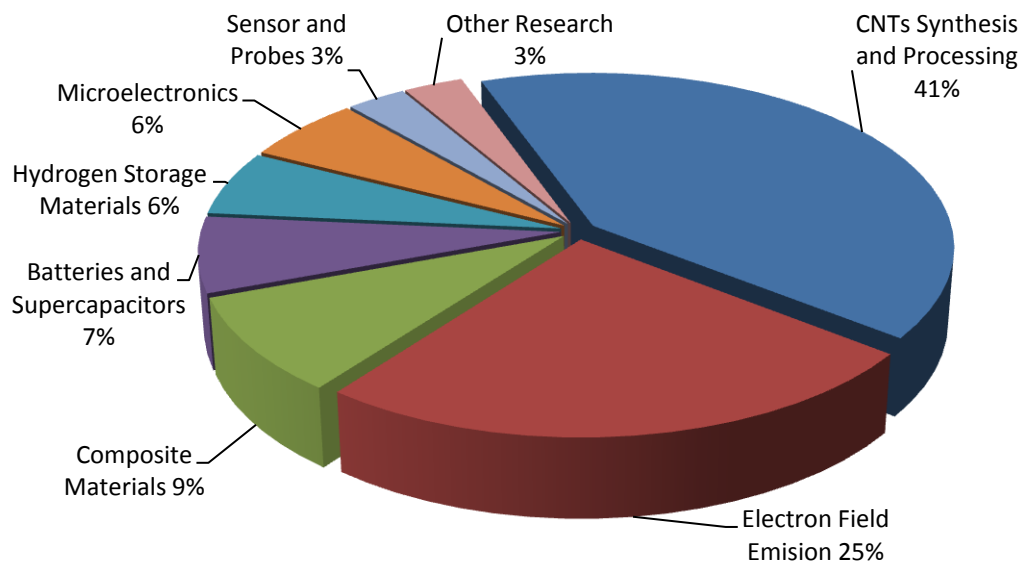
Figure 2.2. CNT-related patents by area of research in 2002 [16].

There are several characteristics that make carbon nanotubes excellent emitting materials. In principle, carbon nanotubes can be considered as a cylindrically rolled sheet of graphite, which is a semiconductor material with zero band gap [16]. Even though this similitude to graphite, CNTs can present either metallic or semiconducting behavior, depending on their specific spatial configuration [16]. This spatial configuration is determined according to the direction in which the graphite sheets are rolled up to form the nanotubes. Three configurations have been determined for carbon nanotubes: armchair, zigzag and chiral configuration (see Figure 2.3). CNTs having an armchair configuration present metal behavior, whereas CNTs with zigzag and chiral configurations behave as semiconductors [11, 16]. In addition to these electronic structure dependent properties, the mechanisms for CNTs production with the desired shape and characteristics are reaching the stage of maturity. Moreover, CNTs have excellent chemical stability and excellent mechanical properties. All of these are desirable properties for field emitter materials. Besides, CNTs have the ability to behave as conducting materials with large aspect ratios, which are key properties that make CNTs excellent candidates for field emission devices.
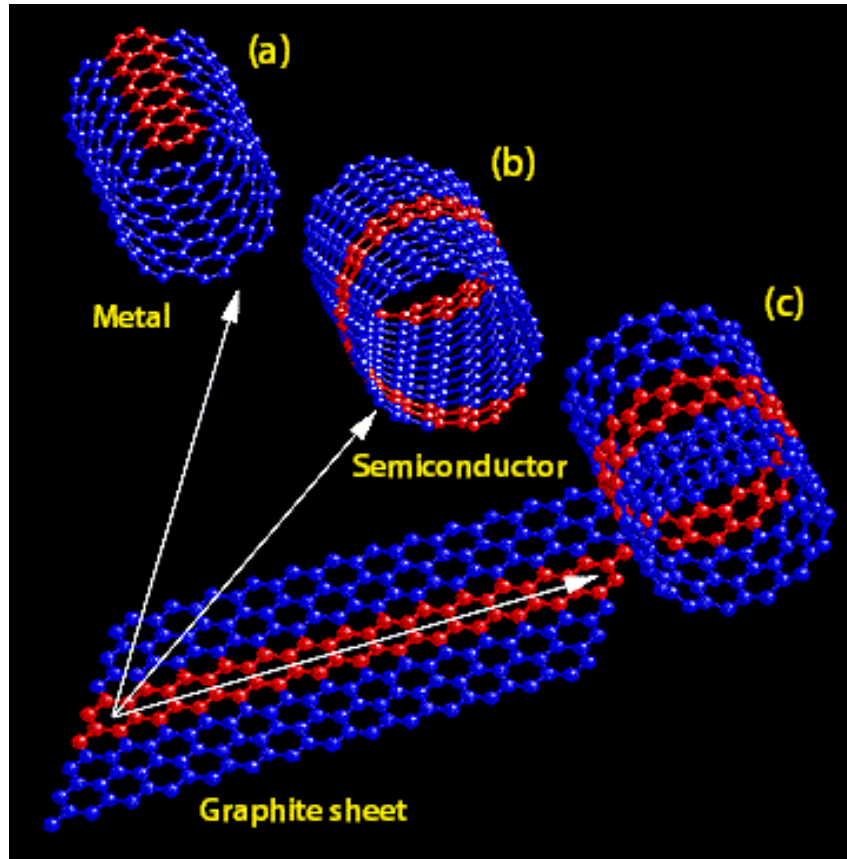
Figure 2.3. Different spatial configurations of carbon nanotubes. (a) armchair, (b) zigzag and (c) chiral [18].

Besides having a metallic structure, conducting CNTs are composed of strong sp^2 covalent bonds. In consequence, the activation energy for the migration of the carbon atoms in the CNTs structure is larger than it is in conventional metallic emitters [19]. This provides CNTs with the capacity of withstand high electric fields required for field emission without further detrimental consequences. In addition, this covalent bond characteristic allows CNTs to support extremely high emission current densities before the covalent bond are broken, such that values as high as $\sim 10^{10}$ A/cm^2 have been reported for CNT systems [11].

As mentioned before, the large aspect ratio of carbon nanotubes is also a key parameter for the field emission from carbon nanotubes. Due to this large aspect ratio, the magnitude of the electric field in the vicinity of the caps of conducting CNTs is enhanced

by either hundreds or thousands of times the magnitude of the externally applied electric field. As a consequence of this electric field enhancement electrons can be emitted from CNTs at low voltages [20].

The *enhancement factor* (β) is be defined according to conventional field emission theory as the ratio between the local electric field at a point in the CNTs (E_X) and the externally applied electric field E ($\beta=E_X/E$). For an isolated carbon nanotube, the enhancement factor is shown to have a power law dependence of the form [3]:

$$\beta = \left(\frac{h}{r}\right)^n \tag{6}$$

Where h is the height and r the radius of the nanotube. A commonly accepted approximation establishes n=1. However, for CNTs the value of n=1 tend to overestimate the real field enhancement over the CNT [3]. On the other hand, when the simulations included more than one CNT, the enhancement factor over each CNT was found to be lower than it would be for an isolated one. This decrease in the enhancement factor for an array of CNTs is denominated *screening effect.*

This field screening effect is illustrated in Figure 2.4. It shows the local electric field distribution for arrays of 11x11 (Figure 2.4-(a)) and 3x3 (Figure 2.4-(b) and (c)) CNTs. As seen in these figures, the magnitude of the local electric field is higher in the tip of the CNTs compared to the rest of their bodies. Furthermore, this field enhancement is non-uniform across the arrays of CNTs. The highest enhancement factor is found in the CNTs located at the edges of the arrays (Figure 2.4-(a)). Due to the screening effect in CNTs assemblies have been reported. These reports the enhancement factor in the tip of the emitters is decreased as the distance between the emitters decreases. This enhancement factor decreases rapidly for distances between the CNTs lower than twice their height [19].
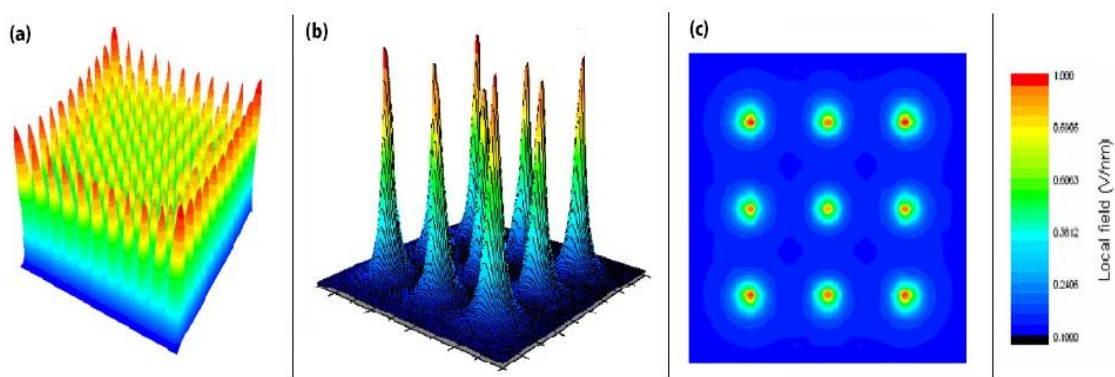
Figure 2.4. Simulated local electric field over different sets of carbon nanotubes. (a) surface plot of an array of 11x11 CNTs, (b) surface plot of an array of 3x3 CNTs spaced 30nm between them, (c) contour plot of the array shown in part (b) [3].

Jonge and Bonard [19] illustrated this screening effect by simulating the equipotential lines of the electric field for both an isolated CNT and an array of several CNTS. Results indicate the "shielding effect" generated by the assembly of CNTs and how the enhancement factor in each of the CNTs in the array is decreased in comparison to the one obtained for a single nanotube (see Figure 2.5).
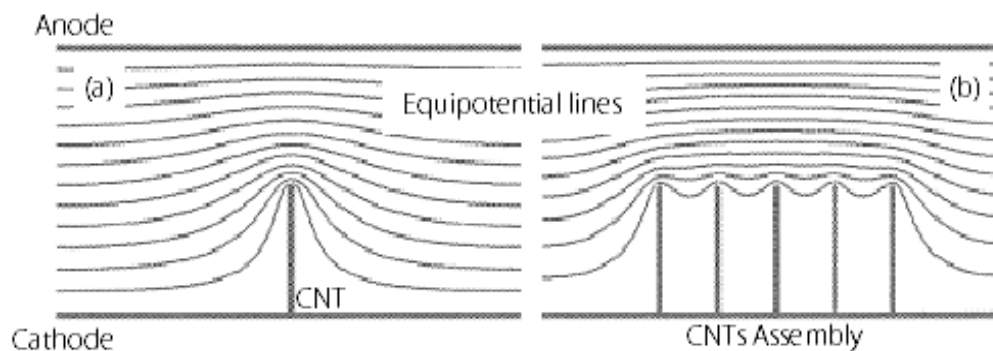
Figure 2.5. Shielding effect. Equipotential lines or the electric field in (a) a single CNT and (b) a linear assembly of five CNTs [19].

As a consequence of the lower enhancement factor, the voltage required for the field emission to ocurr will be higher for a bundle of CNTs than for an isolate nanotube, as it was shown experimentally by Jonge and Bonard [19]. They reported that only 90V were required for field emission to occur in a single CNT, whereas at least 200V were necessary for the emission of electrons to be observed in a bundle of CNTs (see Figure 2.6). These results indicate the existence of an optimum distance between CNTs in an emitting array for which the emission current density will be optimum. This optimum separation has been found to be twice the height of the CNTs [3, 17, 19]. Despite the screening effect, carbon nanotubes are still considered excellent alternatives as field emitter materials. In Table 2.1 the electric field threshold required for to obtain an emission current of 10mA/cm^2 from different materials is presented. The materials presented in this table have typical work functions (Φ) in the order of 4.5 to 5eV. A comparison between CNTs and the other emitter materials considered in Table 2.1 indicates the superior capacity of CNTs to emit electrons at low electric fields. In order to obtain an emission current in the order of 10mA/cm^2, electric fields in the range of 1-5 V/μm are required for CNT systems. To obtain a similar emission current density from a metal with a flat surface, the threshold field will be in the order of 10^4 V/μm.
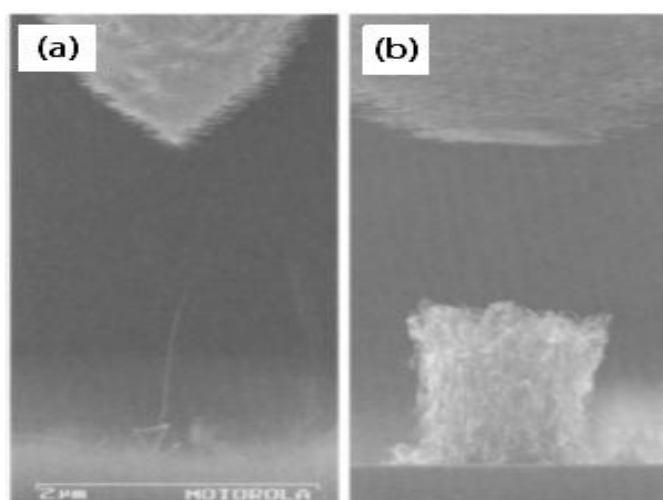
Figure 2.6. Field emission evaluated in (a) an isolated CNT and (b) a bundle of CNTs. Emission of electrons from the isolated CNT was observed at 90V, whereas at least 200V where necessary for emission to occur in the bundle of CNTs [19].

Table 2.1. Electric field threshold required for an emission current density of 10mA/cm^2 from different emitter materials [5].

Emitter Material	Threshold field [V/µm]
p-type diamond	70-100
Silicon tips	70-100
Rare earth salt coated polycrystalline diamond	20-25
Graphite coated silicon tips	10-15
Nano-diamonds	3-5
CNTs	1-5

2.3 FOWLER-NORDHEIM CHARACTERISTICS OF CNT EMITTERS

Since 1995 when field emission of electrons from CNTs was first reported [17], their field emission characteristics have been extensively studied. A two parallel electrodes structure (diode) is usually employed on the analysis of the field emission characteristics of CNT samples. This diode structure is composed of a CNT-based cathode where the emission of electrons occurs, and an anode used to extract the electrons. Electrodes are set at a distance d and a potential V is applied between them for the emission of electrons to occur (see Figure 2.7).

To characterize the field emission in these diode structures, the emission current (I) is measured at different voltages (V), and results are used to construct the characteristic I-V curves of the system. Results obtained are then compared to the Fowler-Nordheim equation to determine whether it is the mechanism behind the emission of electrons [2]. This comparison is made by plotting the parameters $\log(I/V^2)$ versus 1/V. If a straight line is obtained, field emission is occurring according to the Fowler-Nordheim mechanism [17].
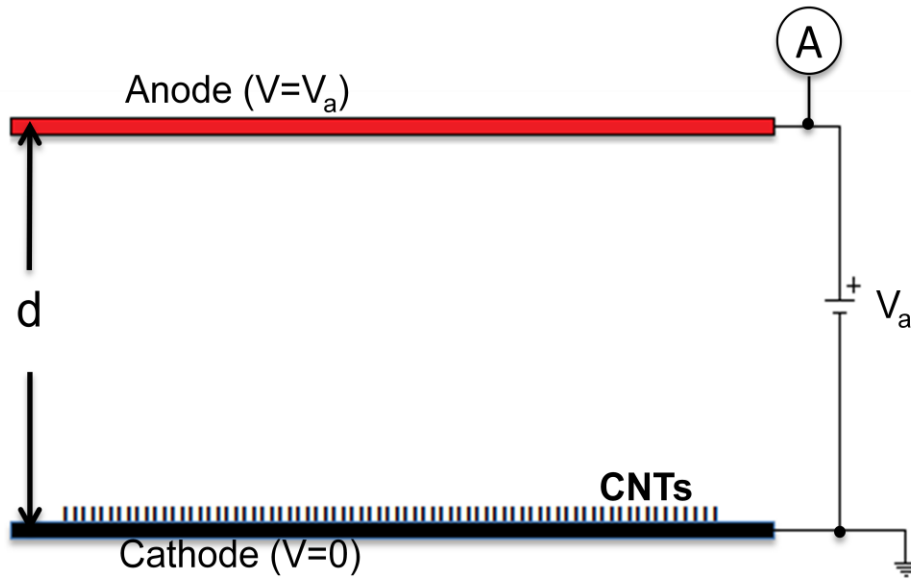
Figure 2.7. Typical diode structure used for field emission measurements.

Furthermore, when a straight line is obtained from the $\log(I/V^2)$ versus $1/V$ plot, the field enhancement factor of the emitter material can be determined (see Figure 2.8) [17].

As shown in Figure 2.8, the emission of electrons from CNTs yields a straight line indicating the field emission from carbon nanotubes occurs according to the Fowler-Nordheim mechanism. Assuming that graphite's work function of 5.0eV is also valid for CNTs, they calculated the enhancement factor of the CNT films used in their experiment to be $\beta=1300$ [17]. Other works reporting the field emission parameters for different CNT samples are found in the literature, some of the reported results are summarized in Table 2.2.
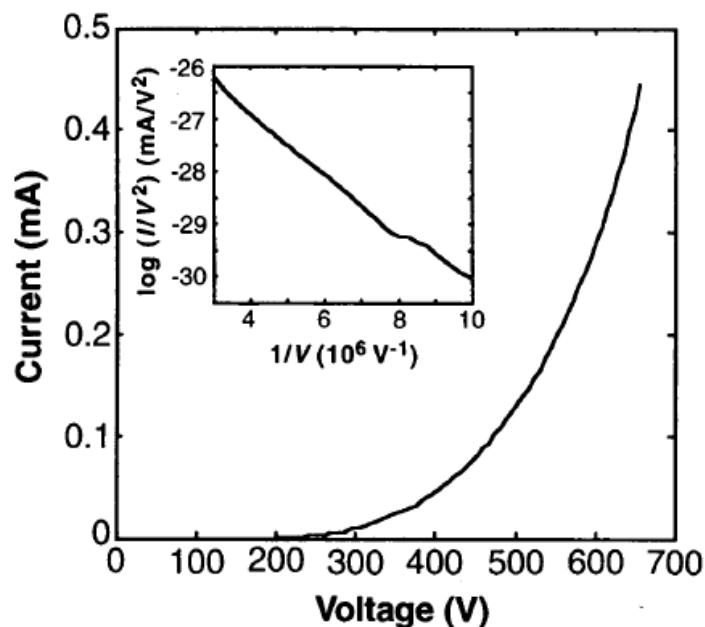
Figure 2.8. I-V curve for emission of electrons from a CNT-based electron source. Emitting area: 1mm². Cathode-anode gap: 20µm. Inside: FN curve - $\log(I/V^2)$ vs. $1/V$ [17].

In general, it has been shown that electrons are field emitted from CNTs according to the Fowler-Nordheim mechanism. It was stated before that the two main factors affecting FN field electron emission are, the work function and the field enhancement of the emitter material. In Table 2.2, values reported for the work function of different CNT samples are between 4.5 and 5.0eV, which are similar to the work function (Φ=5.0 eV) determined for graphite. On the other hand, values reported for the field enhancement factor (β) of the CNT samples, go from a few hundred to several thousands. This variation in β values is usually attributed to methodology used to synthesize and fabricate the CNTs-based cathode. Moreover, it was established in a previous section that variables such as the aspect ratio of the CNTs and the separation between them in the emitter array influence the enhancement factor. These different variables were taken into account in the selection of the Fowler-Nordheim parameters used in the simulations presented here. As a result, the emission of electrons from the

CNTs is simulated according to the Fowler-Nordheim mechanism, with Φ= 5.0 eV and β=2200.

Table 2.2. Fowler-Nordheim parameters for the field emission of electrons from different CNT samples.

Emitter Type	Work Function (Φ) [eV]	Enhancement factor (β)	Source
CNT film	5.0	1300	[17]
CNTs grown in a TiCN substrate	5.0	992	[21]
CNT film	4.5	1000	[22] [23]
Printed CNT cathode	4.5-5.0	2265	[24]
CNTs grown in a Ni Substrate	4.7	1100	[25]
SWNT $\approx$10µm bundle length	4.8	2423	[26]
CNT film grown in Ag-past	5.0	5228-7000	[27]

3. METHODS

3.1 THE TRIODE STRUCTURE

In order to understand the electron field emission characteristics of the proposed CNT-based flat panel X-ray source, a triode structure is used to simulate the emission of electrons in a single x-ray source. The Particle-In-Cell code OOPIC Pro is used for the simulations. OOPIC Pro is a two dimensional PIC code developed to simulate the interaction between plasmas and beam of charged particles with externally generated field [29]. In order to provide realistic results for the simulations of systems with high number of interacting particles, the PIC algorithm uses the concept of "macroparticles". Using this concept, the PIC algorithm simulates the energy, velocity and position characteristics of $\sim 1 \times 10^6$ particles by using a macroparticle with equivalent electric and physical characteristics. Without using this PIC approach, the simulation of systems like the one simulated in this thesis become highly computational demanding problems due to the high number of particles and interactions to be taken into account at a given time [29].

In this chapter, the methods, parameters and geometries used for the simulations are presented. The simulated triode structure used has three basic components: *cathode, extraction grid and anode*. The walls of the cell are simulated as *insulators*. Experimentally, these insulators will be used as separators between the cathode, the extraction grid and the anode. In order to evaluate their effect on the trajectory of the emitted electrons, a set of *focusing lens* was added to the triode structure. The array of *CNT field emitters* located at the cathode is simulated according to the *Fowler-Nordheim* mechanism. A low voltage bias (20-70 V) is applied to the extraction grid (*extracting voltage)* is used to extract the electron from the CNT emitters. The emitted electrons are accelerated toward the anode using a high voltage bias applied between the cathode-anode gap (*accelerating voltage*). The emission of electrons is simulated for extracting voltages between 0 and 70 V, and accelerating voltages between 30kV and 120kV. Furthermore, the trajectory and field emission characteristics have been evaluated for the cases where 4kV and 14 kV were applied to the focusing lens. A diagram of the triode structure used for the simulations is presented in Figure 3.1.

In the proposed design, transmitted x-rays are generated by Bremsstrahlung interactions between high energy electrons and a target material located at the anode. The Monte Carlo code MCNPX has been used to evaluate the x-ray generation characteristics of the proposed structure. Results of the MCNPX simulations of the x-ray generation characteristics of the proposed structure are reported elsewhere [28].
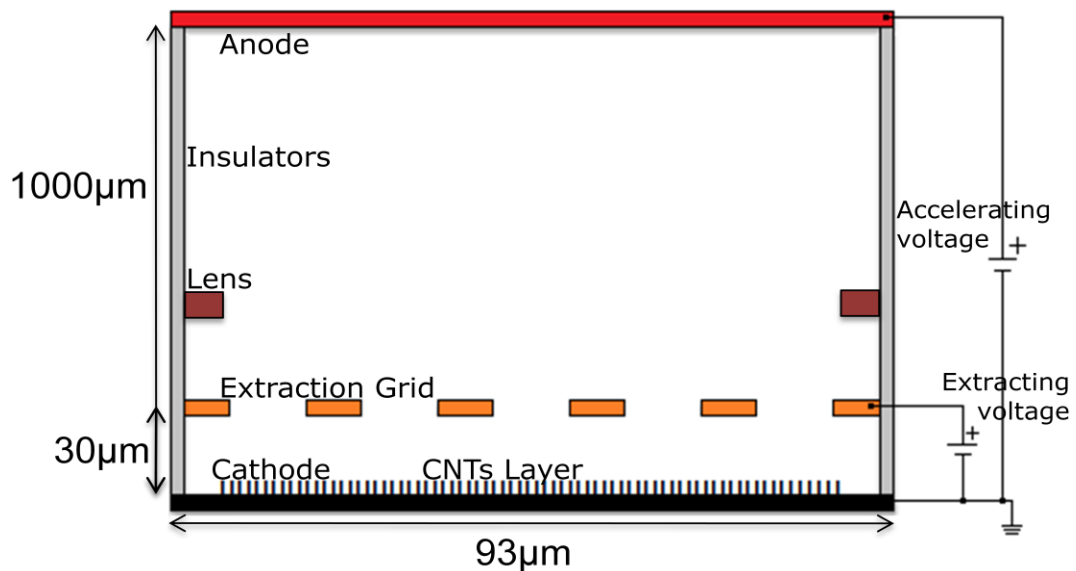
Figure 3.1. Triode structure used for the field emission simulations

3.2 THE OOPIC PRO MODEL

OOPIC Pro is a relativistic two dimensional particle in cell code developed to simulate the interaction between plasmas and beams of charged particles with externally generated fields [29, 30]. Using OOPIC Pro, the triode structure presented in Figure 3.1 has been modeled. The components of the triode structure were described in the previous section and are defined in OOPIC Pro as boundary surfaces. The types of boundary surfaces used to represent each component of the triode structure have been selected according to the expected electrical properties of these components. In consequence,

cathode, extraction grid, anode and focusing lens are defined as equipotential boundary surfaces. In OOPIC Pro, equipotential surfaces behave as perfect conductors grounded at a specific potential, this potential can be fixed or defined as a function of time [30]. The insulators or walls of the triode structure were simulated as dielectric boundary surfaces. The accumulation of charges due to electrons striking the surface of the dielectric surfaces is taken into account in the OOPIC Pro model [30]. Emission of electrons from the CNT emitters located at the cathode was modeled according to the FN mechanism discussed before (see equation (1)) [2]. The FN mechanism is an OOPIC Pro built-in function, which is called by incorporating the "FowlerNordheimEmitter" block in the input file (see Appendix) [30]. The input parameters for this "FowlerNordheimEmitter" were selected according to common values reported for the emission of electrons from CNTs (see Table 2.2). These input parameters include, the work function (Φ) and the field enhancement factor (β) of the CNTs. A screenshot of the actual geometry modeled in OOPIC Pro is shown in Figure 3.2, in which the x-y phase space output of one of the simulations run in OOPIC Pro is seen. The components of the simulated triode structure are indicated in Figure 3.2. In this figure, emitted electrons are seen as a sequence of dots next to the surface of the cathode.
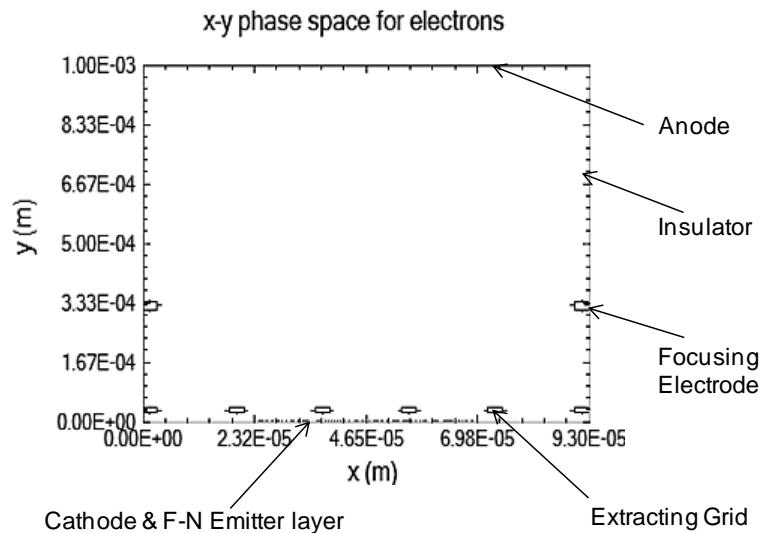
Figure 3.2. Screenshot of actual geometry modeled in OOPIC Pro.

Details of the cathode- anode and cathode-grid distances as well as the different grid and anode voltages used for the simulations are presented in Table 3.1. The cathode-anode distance was selected such that for anode potentials in the range of 30 to 120kV, no extraction of electrons will occurs due to the anode potential. For the geometric characteristics considered for the grid, the minimum cathode-anode distance was found to be 1000 μm. For this distance, the emission of electrons is controlled by the voltage applied to the extraction grid.

A pixel size of 100x100μm has been proposed for the original design. This pixel size corresponds to the width and depth of each of the proposed micro x-ray cells. Taking into account this proposed pixel size and due to geometrical limitations of the code implemented in OOPIC Pro, the pixel size (width) selected for our simulations is 93μm. Since OOPIC Pro is a two dimensional simulation code, the third dimension cannot be defined in the input file. However, for the calculations, OOPIC Pro assumes the third dimension to be equal to 1 m (z = 1 m).

Table 3.1. Geometric and electric parameters used for the OOPIC Pro simulations

Parameter	Value
Cell width	93 μm
Cathode to Anode Distance	1000 μm
Cathode to Grid distance	25 μm
Grid Aperture	15 μm
Grid Width	3 μm
Grid Thickness	12.5 μm
Cathode Voltage	0 V – (Ground)
Grid (Extracting) Voltage	20 - 70V
Anode (Accelerating) Voltage	30, 40, 60, 80, 100 and 120 kV
Focusing lens Voltage	4kV (30kV Case) and 14kV (120kV Case)

The geometric characteristics of the extraction grid were selected according to the dimensions of commercially available transmission electron microscopy (TEM) grids. These commercially available TEM grids are planned to be used for the constructions of a first prototype of the proposed device. A diagram with the geometric characteristics of the extraction grid is presented in Figure 3.3.
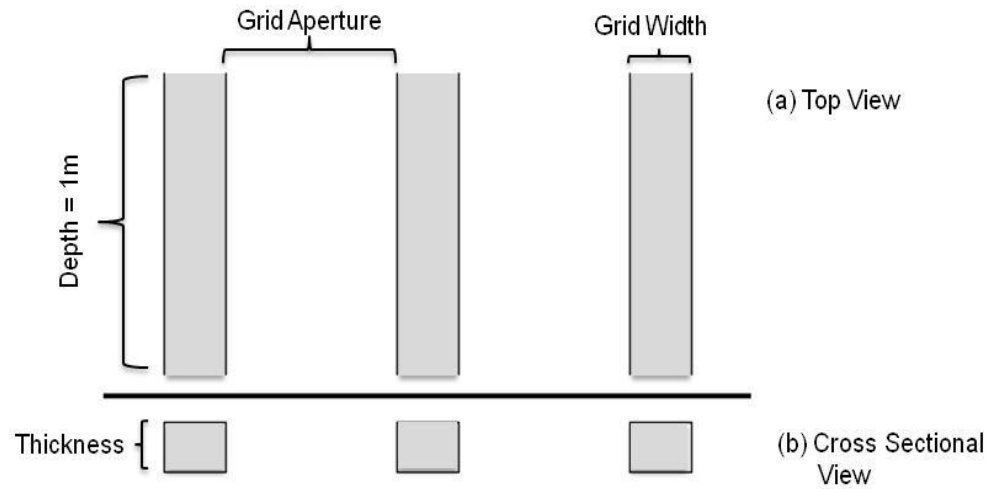
Figure 3.3. Dimensions defined for the extraction grid in the PIC 2D simulation. Diagram not to scale

Moreover, the FN parameters used to simulate the emission of electrons from the CNTs are shown in Table 3.2. (See Table 2.2 for further details). The FN emitters are located on top of the cathode surface, simulating a layer of CNTs grown or deposited in this boundary surface. The OOPIC Pro input file has been set in such a way that the emitting layer is centered and covers 50% of the total surface of the cathode.

Table 3.2. Fowler-Nordheim parameters used in the OOPIC Pro simulations

FN Parameters	Value
Work Function (eV) Φ_w	5
Field Enhancement β_{FN}	2200
A_{FN}	1.5415 x 10^{-6}
B_{FN}	6.830 x 10^9
C_v	0
C_y	3.79 x 10^{-5}

In Particle-In-Cell (PIC) simulations, defining the right spatial and temporal resolution is important to guarantee the stability of the code and the accuracy of the results. Due to the characteristics of the PIC algorithm, it is required to guarantee that particles will not advance more than one cell per time step. However, cells and time steps must be small enough so that sufficient details are revealed by the OOPIC Pro simulations with errors as small as possible [29]. In the simulations here presented, 31 and 80 cells were used in the x- and y-directions respectively. It gives us a spatial resolution of $dx = 3\mu m/cell$ and $dy12.5\mu m/cell$. Regarding the temporal resolution, the time step (t_{step}) has been defined as:

$$t_{step} = 0.5 * dy/c = 2.084 \times 10^{-14} \ s, \tag{7}$$

In this equation, c corresponds to the speed of light, $c = 2.99792458 \times 10^8 m/s$. This condition establishes that any particle going as fast as the speed of light will travel only half of the distance dy, with dy being defined as the spatial resolution in the y-direction. Additionally, in order to guarantee convergence and stability of the PIC algorithm, the denominated Courant-Lewly stability criterion needs to be satisfied.

For the simulations presented in this work, an electrostatic solver has been selected; and the Courant-Lewly Criterion was guaranteed, such that particles will not jump more than one cell per time step [29]. For further details, the OOPIC Pro input file used in the simulations can be found in the Appendix.

4. RESULTS AND DISCUSSION

In this section, results obtained from the OOPIC Pro simulations are presented. Simulations were run for the conditions stipulated in Table 3.1. Results presented in this section include: 2-D particle position and 2-D electric-field vector plots including the effect of focusing structures. Also, anode current densities are determined for different grid and anode voltages (J_{FN}-V curves). Furthermore, the energy distribution of the electrons reaching the anode is presented at various accelerating voltages. A correlation between the anode voltage and the energy of electrons at anode is determined as well. Also, the effect of adding focusing lens on the focal spot size of the electron beam is analyzed.

4.1 TOTAL NUMBER OF PARTICLES AND CONVERGENCE

The total number of particles in the system at a given time was determined for each of the simulations. In each case, results for the total number of particles in the system was used as the main convergence criteria. Only the particles inside the triode structure were considered as part the simulations. Once particles reach any of the surfaces of the triode structure, they are not considered part of the system anymore. In the proposed model, neither secondary emission nor reflection of particles in the surfaces of the triode structure were considered. Therefore, the layer of CNT emitters located at the cathode is the only source of particles (electrons) in the system. Also, no net accumulation of particles or total energy can occur in the system during steady operation condition. Figure 4.1 summarizes the behavior of the total number of particles in the systems as a function of time. In the model used for the simulation, the DC voltage applied to the extracting grid (25 – 70 V) is considered to have a rise time equal to 10 ps. This is the time required for extracting grid potential to go from 0 V to the value set in each simulation. Therefore, no emitted electrons are initially present in the system and the number of particle remains close to zero during the first $1x10^{-11}$s. Around $1x10^{-11}$ s, the grid voltage is high enough for the emission of electrons to occur and the number of particles in the system starts increasing rapidly until it reaches a maximum. The time at

which the number of particles in the system peaks indicates the moment at which the first electrons emitted from the cathode reach the anode surface.

In the case presented in Figure 4.1, the maximum number of particles is reached around 4.2×10^{-11} s. After the number of particles reaches its maximum, it remains fairly constant over time at a value around 7×10^7 electrons. It indicates that equilibrium between the number of electrons being emitted from the cathode and the number of electrons leaving the system through the surfaces of the triode structure is established. This constant value in the number of particles reaching the anode at a given time will determine the current density of electrons striking the anode/target during steady operation conditions. If no convergence is reached in the simulations, the total number of particles in the system continues growing without reaching a maximum point. This behavior indicates the presence of non-physical phenomena in the simulations. The growing trend for the number of particles in the system will continue until the code finally crashes due to the high number of particles in the system. If no convergence is achieved, collected results must not be taken as an appropriate representation of the real physical problem.
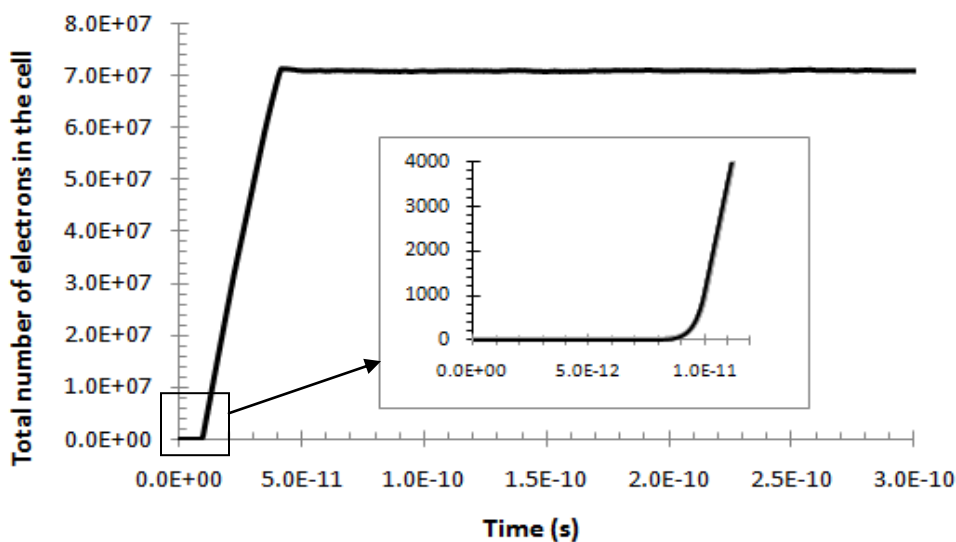
Figure 4.1. Total number of emitted electrons in the triode structure as a function of time. Grid voltage: 42V, anode voltage: 30kV, no focusing.

4.2 ELECTRON TRAJECTORIES AND FOCUSING CHARACTERISTICS

Following the determination of the convergence and physical significance of the simulations, trajectories of the emitted electrons were determined. These electron trajectories were determined with and without focusing lens being included in the triode structure. In Figure 4.2 a typical trajectory of the beam of emitted electrons is presented.
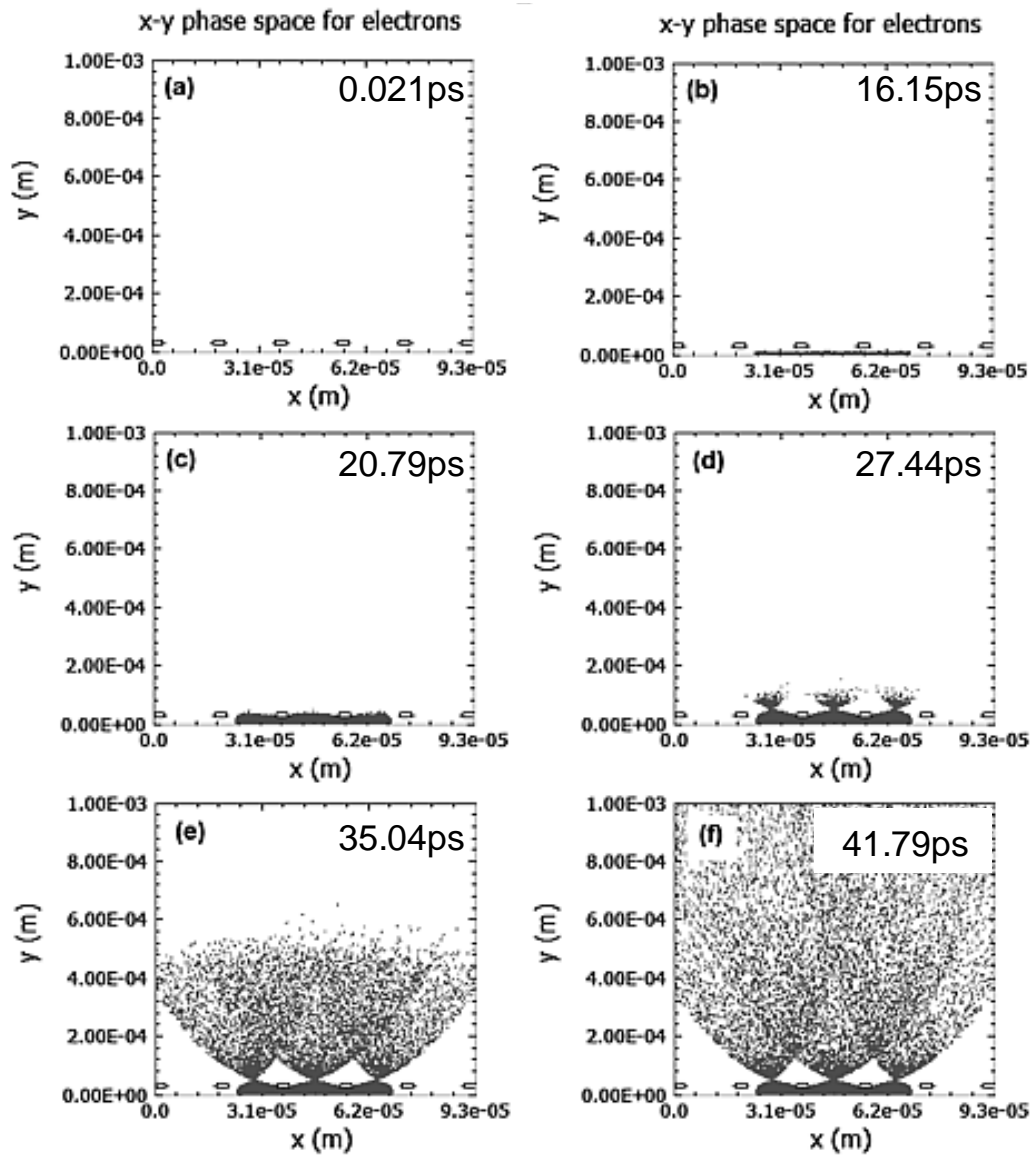
Figure 4.2. Trajectory of the beam of electrons without focusing. Grid voltage: 45V, anode voltage: 30kV, no focusing.

As shown in Figure 4.2-(a), no particles are initially present in the system. However, as time goes on, the emission of electrons due to the electric field generated between the cathode-grid gap begins (Figure 4.2-(b)). In the vicinities of the extraction grid, the trajectory of emitted electrons was found to follow a convergent trajectory such that a crossover of the beam of emitted electrons is observed (Figures 4.2-(c) and -(d)). This crossover observed in the trajectory of electrons is associated to a distortion of the electric field lines in the surroundings of the extraction grid (see Figure 4.3). This convergent behavior observed for beams of field emitted electrons in triode structures has been reported before by D.M. Garner [31]. In his work, Garner modeled a simple triode structure and determined the trajectory of electrons using a Runge-Kutta algorithm. In agreement with the results presented in this work, Garner found the crossover of the electron beam to be associated with the distortion of the electric field around the edges of the extraction grid. This distortion is also associated to a self-focusing effect observed for electron beams accelerated at voltages much lower (~600V) than the ones considered in this thesis [31].
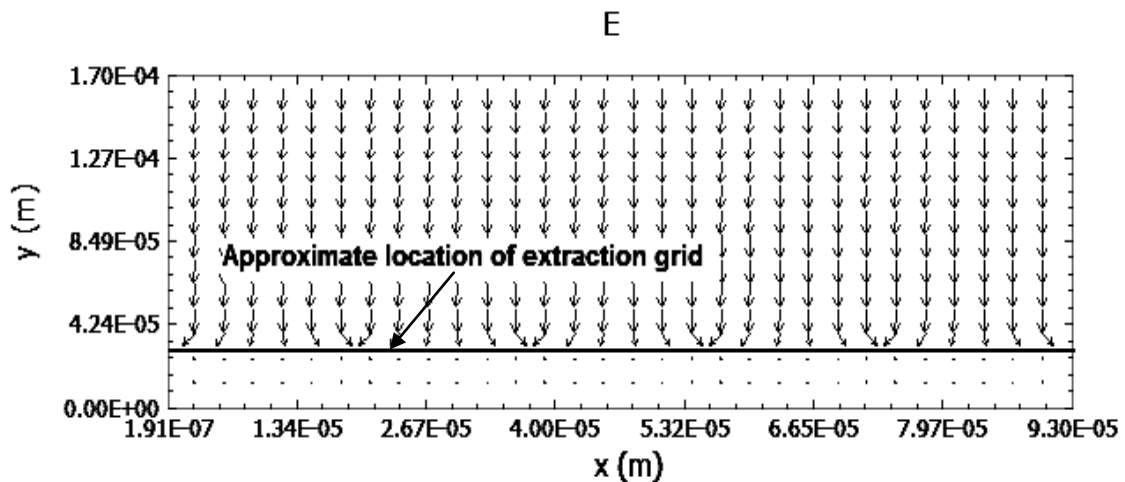
Figure 4.3. Electric field in the vicinities of the extraction grid. Arrows indicate qualitatively the dimension and direction of the electric field at each of the nodes used by the PIC algorithm. Grid voltage:42V; anode voltage: 30k; no focusing.

As shown in Figure 4.2-(e), electrons tend to keep the divergent trajectory acquired after they pass the "crossover" region. This divergent trajectory continues until they are collected on any of the surfaces of the triode structure. Figure 4.2-(f) shows that some of the emitted electrons do not reach the surface of the anode and are collected on the walls of the triode structure instead. In addition, it can be seen that electrons reaching the anode are distributed over the whole surface of it. In consequence, the highly divergent trajectory of the electron beam will lead to both accumulation of charges in the walls of the triode structure and a large focal spot size. In order to mitigate these potentially negative effects on the operation of the proposed electron source, the possibility of using focusing lens to control the trajectory of the beam of electrons was analyzed. Typical results for the electron trajectory when focusing electrodes are added to the triode structure are presented in Figures 4.4-(a) through -(f).

As seen in Figures 4.4-(a) through -(d), the initial electron trajectory when focusing electrodes are present in the triode structure is similar to the electron trajectory observed when focusing electrodes are not present (Figures 4.2-(a) through -(d)). However, it is observed that the presence of focusing electrodes changes the electron path from a divergent trajectory to a convergent one (Figures 4.4-(e) and -(f)). It indicates that using focusing electrodes both the accumulation of charges in the walls of the triode structure and the focal spot size of the electron beam at the anode can be effectively controlled. As in the cases where no focusing lens where used, the change in electron trajectories when focusing lens are added to the simulations are associated to distortions in the electric field lines. Similar to Figure 4.3, Figure 4.5 is a qualitative representation of the direction and magnitude of the electric field in the vicinities of the extraction grid when focusing electrodes are used.

This equivalence in the electric field lines provides a better understanding of the similarity of the initial electron trajectories with and without focusing electrodes. On the other hand, the focusing effect is clearly seen in later stages when the beam of electrons passes through the focusing electrodes.

x-y phase space for electrons

x-y phase space for electrons

(a) 0.021ps

(b) 17.55ps

(c) 26.46ps

(d) 38.88ps

(e) 41.09ps

(f) 48.16ps
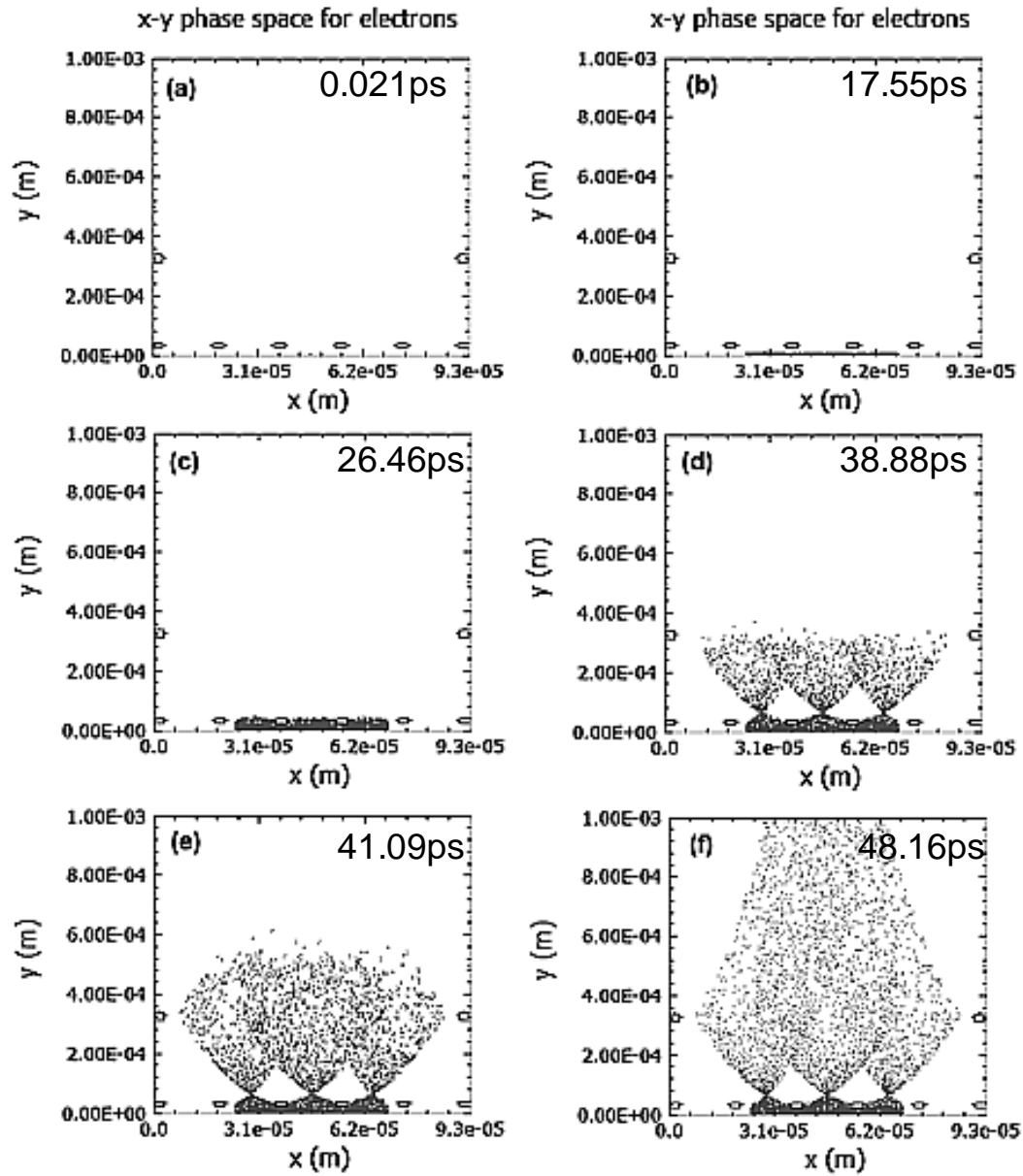
Figure 4.4. Trajectory of the beam of electron with focusing. Grid voltage: 45V, anode voltage: 30kV, focusing voltage: 4kV.

The electron beam goes from a clearly divergent trajectory to a convergent one (Figures 4.4-(e) and -(f)). The reason for this change in trajectory is given by the distortion of the lateral component of the electric field in the vicinities of the focusing electrodes as indicated qualitatively in Figure 4.6.
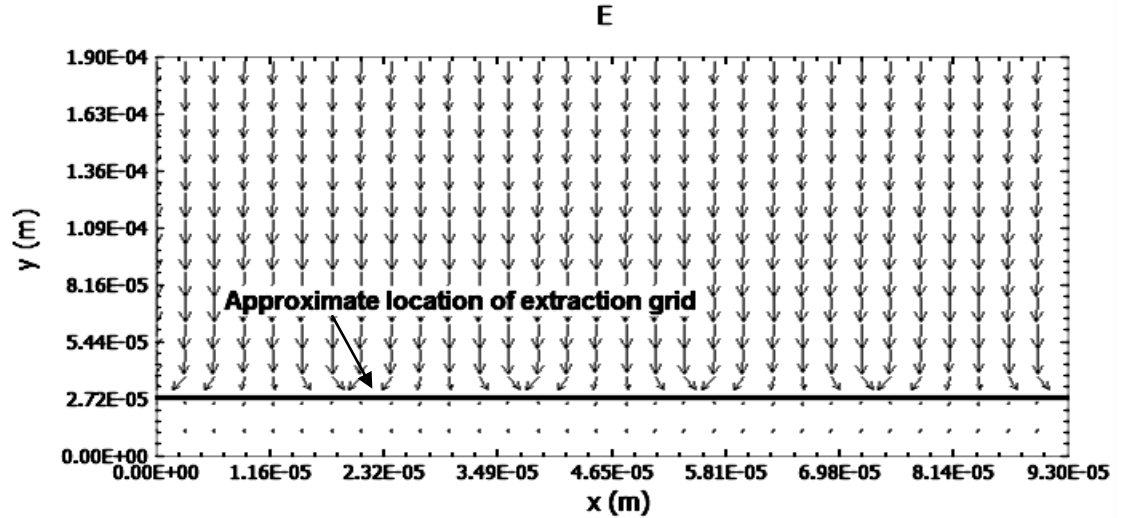
Figure 4.5. Electric field in the vicinities of the extraction grid. Arrows indicate qualitatively the dimension and direction of the electric field at each of the nodes used by the PIC algorithm. Grid voltage: 42V; anode voltage: 30kV; focusing voltage: 4kV.
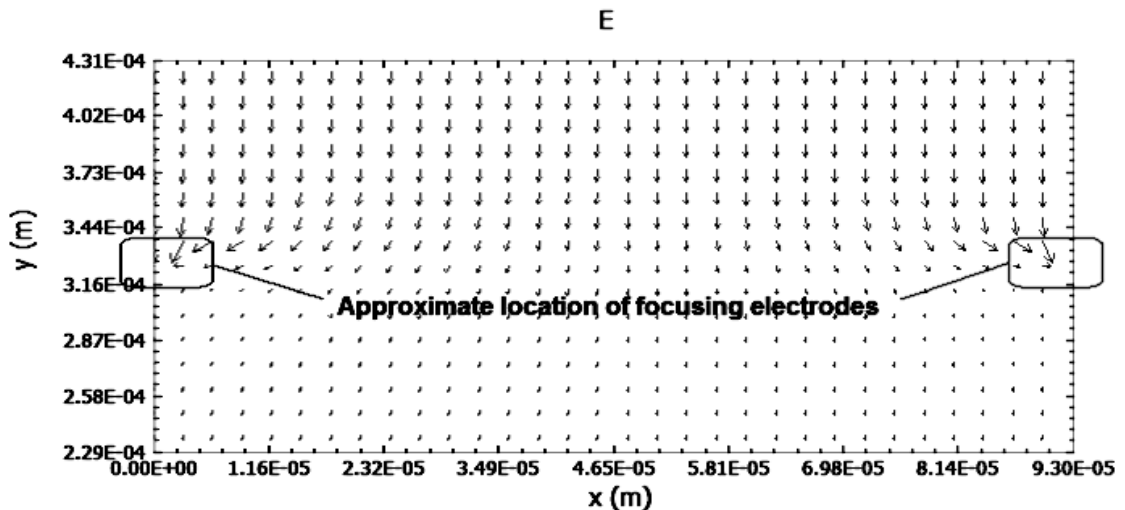
Figure 4.6. Electric field lines in the vicinities of the focusing electrodes. Arrows indicate qualitatively the dimension and direction of the electric field at each of the nodes used by the PIC algorithm for the calculations. Grid voltage: 42V; anode voltage: 30kV; focusing voltage: 4kV.

4.3 CURRENT DENSITY VS. EXTRACTING VOLTAGE: J_{FN}-V CURVES

Two important variables in the design and operation of x-ray sources are the number and the energy distribution of x-rays produced at the anode at any given time. These two variables are associated with the number and energy distribution of the high energy electrons striking the x-ray target. In this section, results including the current density (mA/mm^2) and energy distribution of electrons striking the anode at a given time are presented as a function of grid and anode voltages. These results are summarized in Figure 4.7, which corresponds to the J_{FN}-V curves of the simulated triode structure. These J_{FN}-V curves correlate the electrons current density at the anode to the applied grid voltage. A J_{FN}-V curve has been built for each of the anode voltages listed in Table 3.1.
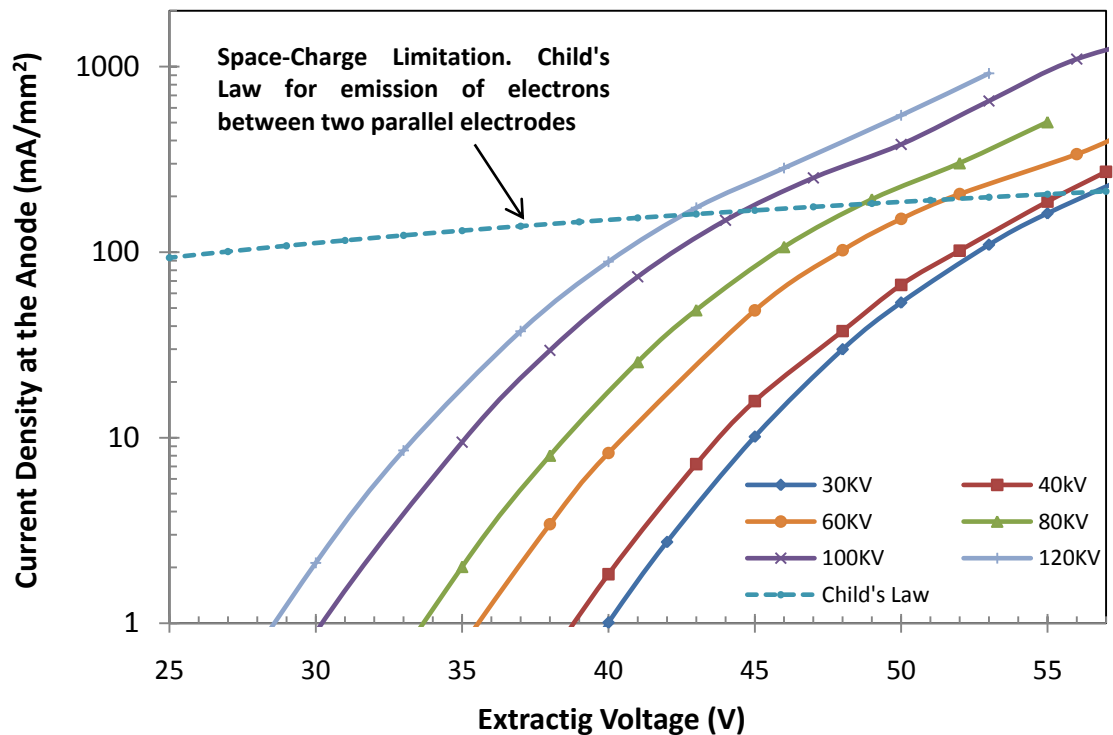
Figure 4.7 J_{FN}-V curves – Anode current density (mA/mm^2) as a function of the grid voltage at different anode voltages. No focusing electrodes present in the triode structure.

Considering the logarithmic scale in the y-axis in Figure 4.7, it is seen that the electron current density at the anode increases rapidly as the grid voltage is increased. This fast increasing behaviour of the current density is characteristic of Fowler-Nordheim emitters and can be explained by the exponential component of the Fowler-Nordheim equation used to model the field electron emission from the CNTs (Eq. (1)).

Furthermore, results presented in Figure 4.7, indicate the existence of an extracting voltage below which no detectable field emission of electrons will occur. This voltage, denominated *turn-on voltage*, has a clear dependency on the voltage applied at the anode. For the 120kV anode voltage case the turn-on voltage was found to be as low as 28.5V, whereas for the 30kV anode voltage case, the turn-on voltage was found to be 40V. This dependency on the anode bias indicates that for a given extracting voltage, the current density will be higher as the anode voltage increases.

For the distances and geometry considered in the simulations, results presented in Figure 4.7 also indicate that the current density is mostly controlled by the grid voltage. This important result leads to the conclusion that the grid voltage can be used to effectively control the emission of electrons in the triode structure; a similar conclusion is reported by Di et. al, [6]. This control of the emission current via grid voltage needs to be guaranteed in order to allow the proposed flat panel x-ray source to be operated in scanning mode in an accurate way. This control via grid voltage will allow the emission of electrons/x-ray generation from each micro x-ray cell in the proposed x-ray source to be controlled independently. This grid control mechanism has been tested and proved from other research groups currently attempting to develop a distributed cold cathode-based x-ray source [23, 24, 25, 32, 34].

-*Space-Charge Limitation:* Results obtained for the current density of emitted electrons as a function of the applied grid voltages indicate that a maximum grid bias can be applied before the current of emitted electrons goes from a continuous process into an oscillatory one. This maximum extracting voltage to be applied is limited by the rapidly increasing behavior of the Fowler-Nordheim emission phenomena. This maximum voltage is also associated with the denominated space-charge limitation phenomena. This space-charge limitation is modeled by the Child-Langmuir law. It establishes that for two parallel plate electrodes, there is a point at which the number of charges is so high that

their electric field will equal the externally generated electric field, reflecting new emitted charges and creating a virtual cathode [33]. In parallel plate electrodes, this charge limitation phenomena or Child-Langmuir's law is determined by the cathode-anode separation and the voltage difference between these two electrodes [33]. Due to the presence of a virtual cathode, the continuous emission of electrons in the system stops and an oscillatory behavior of the emission of electrons is observed instead [33]. This transition from continuous to oscillatory emission of electrons is seen in Figures 4.8-(a) through-(d). In Figure 4.8-(a) a low extracting voltage is applied (30V), so that the number of emitted particles emitted in the systems is low and no space-charge limitation is present. As grid voltage is increased, the number of charges in the system increases as well, and the space-charge limitation phenomenon becomes more significant. In Figure 4.8-(b), a 40V extracting voltage is applied. In this case, the electron current density peaks when the first electrons reach the anode, and then this current stabilizes at a lower value. The maximum value for the current density is obtained for conditions in which no charged particles were initially present in the system. The lower value at which the current density stabilizes takes into account the presence of other charged particles in the system. As a consequence, the difference between the maximum current density and the value at which it stabilizes is attributed to space-charge limitation phenomena induced by the beam of emitted electrons present in the system. Up to this point, the emission of electrons can still be taken as continuous and space-charge limitation phenomena are not significant. On the other hand, in Figures 4.8-(c) and -(d) an oscillatory behavior of the current density is observed. These results were obtained for an anode voltage equal to 100kV and grid voltages of 50 and 56 V respectively. The oscillatory behaviors presented in these figures are a clear indication of the presence of *virtual cathodes* that limits the maximum current that can be extracted from field emitters. These results are in agreement with results presented in Figure 4.7, where Child-Langmuir's law is plotted and is seen as a fairly horizontal line (The reader should be aware of the logarithmic scale used in the graph for the y-axis).
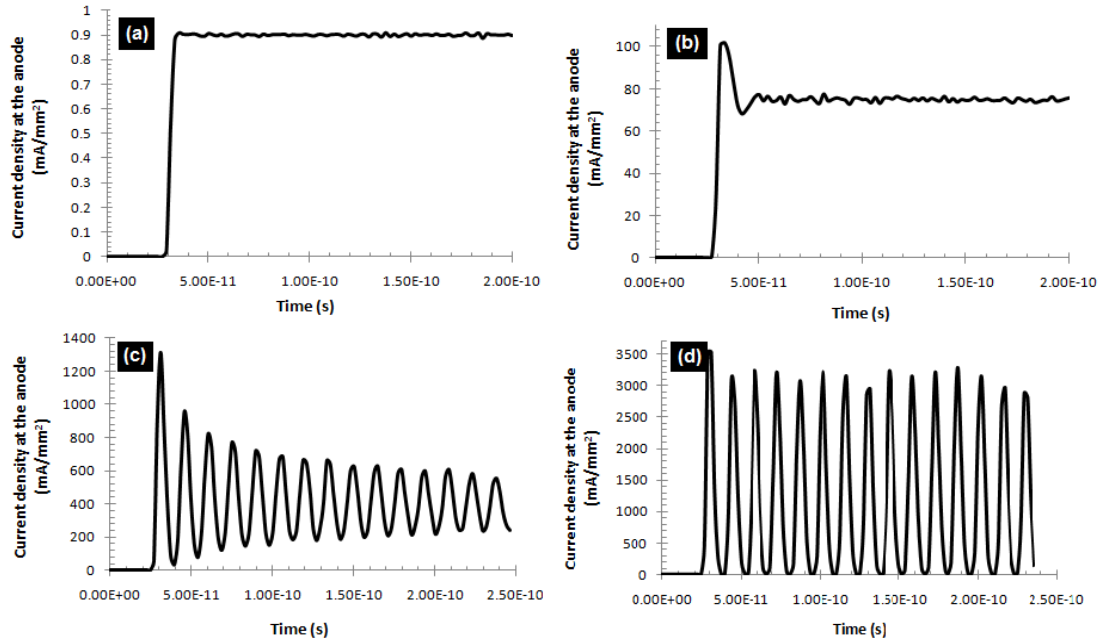
Figure 4.8. Current density at the anode as a function of time. As grid voltage is increased, the system experiences a transition from continuous emission of electrons into oscillatory emission of electrons (space-charge limitation). Anode voltage: 100kV; grid voltage (a) 30V, (b) 41V, (c) 50V and (d) 56V. No focusing.

In Figure 4.7, for a 100kV anode voltage case, the Child-Langmuir's plot indicates that the space-charge limitation phenomena will become significant at grid voltages above 46 V. Depending on the anode voltage, the *space-charge* limitation was found to become significant for simulated systems at grid voltages between 43 and 58V. This is a good benchmarking for the simulated model. In general, the lower the anode voltage, the higher the grid voltage at which space-charge limitation phenomena become significant and the transition from continuous to oscillatory emission of electrons is observed. In Figures 4.9–(a) and –(b), the trajectory of electrons is presented for two systems featuring continuous and oscillatory emission of electrons, respectively.
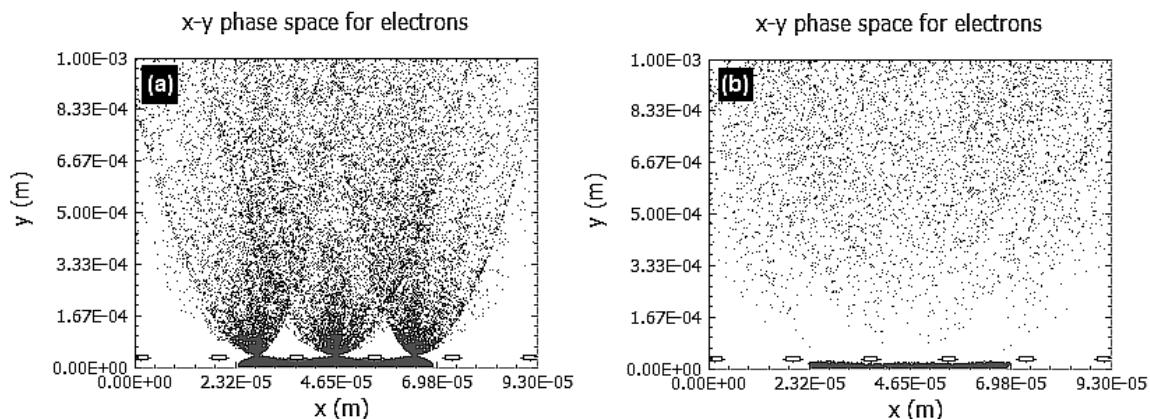
Figure 4.9. Electron trajectory in the triode structure. Anode voltage: 100kV, (a) grid voltage: 35V - continuous emission of electrons, (b) grid voltage: 55V - oscillatory emission of electrons -

4.4 ENERGY DISTRIBUTION OF ELECTRONS REACHING THE ANODE

As mentioned before, two important variables of design and operation of x-ray sources are the amount and energy distribution of x-rays produced at a given time. These two variables are correlated to the amount and energy distribution of electrons striking the x-ray target. In previous sections, electron trajectories have been presented for different simulation conditions. Furthermore, the number of electrons stricking the target have been evaluated in terms of the current density of electrons at the anode surface at a given time. In this section, attention will be focused on the energy distribution of electrons reaching the anode. Results obtained when no focusing lens are included in the triode struture are compared to results obtained when focusing electrons are added to the triode structure. In Figure 4.10, energy distributions of electrons striking the target for focused and unfocused structures are presented. Results showed in Figure 4.10 were run for an anode voltage of 120kV and a grid voltage of 40 kV. In Figures 4.10-(b) and -(d) a focusing voltage of 14kV was applied.
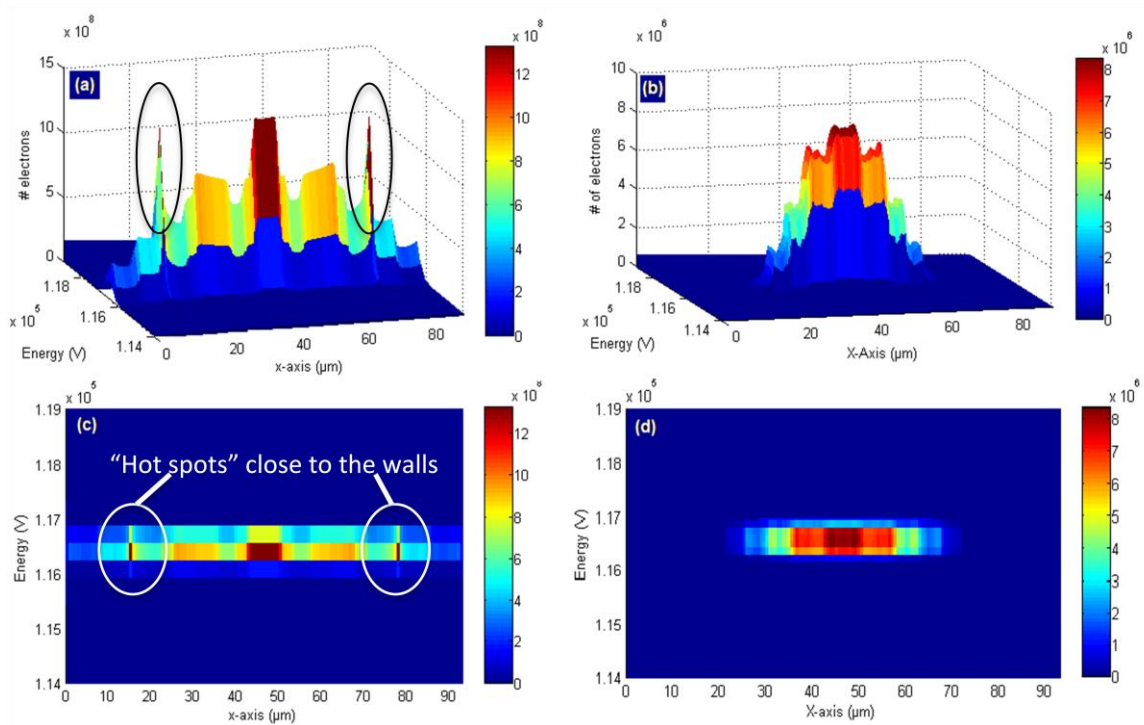
Figure 4.10. Energy distribution of electrons striking the anode. Simulation conditions: Anode voltage:120kV, (a) grid voltage: 40V, no focusing, 3-D view, (b) grid voltage: 40V, focusing voltage: 14kV, 3-D view, (c) same conditions as (a), top view. (d) same conditions as (b), top view.

From the analysis of the electron trajectories, it was established that in the cases where no focusing electrodes are present in the triode structure, the beam of emitted electrons has a divergent trajectory (see Figure 4.2Figure). As a consequence of this divergent trajectory, electrons reaching the anode are distributed over the whole anode surface. Figure 4.10-(a) shows a typical distribution of electrons at the anode. In this figure, the z-axis indicates the number of electrons reaching the anode and the x-axis indicates the position in which the electrons are hiting the anode at a given time. Results indicate a non-uniform distribution of electrons, and some "hot spots" are observed in the center of the anode surface and approximately 20μm away from each of the walls of the triode structure. On the other hand, in the cases where focusing electrodes are present in the triode structure a more uniform distribution of electrons is obtained (Figure 4.10-(b)). In this case, the number of electrons striking the anode reaches its maximum at the center

and decreases gradually toward the edges of the surface. This behavior of the distribution of electrons is associated to the convergent trajectory acquired by the beam of emitted electrons when it passes through the focusing lens (see Figure 4.4).

In addition, the thickness of the 3-D plots presented in Figures 4.10-(a) and-(b) correspond to the energy distribution of electrons reaching the anode. These energy distributions are better illustrated in Figures 4.10-(c) and -(d). These figures can be taken as a top view of Figures 4.10 (a) and (b) respectively, with the color map representing the number of electrons of a given energy reaching the anode at any particular spot in the x-direction. Results presented in Figure 4.10 were obtained from simulations run at an anode voltage equal to 120kV, with and without focusing. In both cases (Figures 4.10-(c) and -(d)), it is seen that the energy of electrons reaching the target is lower than the 120kV potential applied to accelerate the electrons toward the anode. In the case where no focusing structures were used, electron energy ranges between 116 and 117 kV (See Figure 4.10-(c)). This energy band is spread over the whole anode surface. On the other hand, when focusing structures are employed, electron energy still ranges between 116 and 117 KV, but the energy band is narrower than in the case without focusing structures (see Figure 4.10-(d)).

Following these results for the energy distribution and according to the triode configuration used in the simulations, the energy of electrons striking the target is controlled via anode voltage. Under ideal conditions, the final energy of electrons will be equal to the high voltage applied to the anode. However, due to them being charged particles, electrons not only interact with the externally applied electric field but they also experience Coulomb interactions among themselves. Due to these multiple interactions experienced by the emitted electrons, their final energy will be lower than the potential applied at the anode. This effect is seen in Figure 4.11, where the average electron energy is plotted as a function of the accelerating voltage. According to this figure, a linear relationship exists between average energy of electrons reaching the anode and the accelerating (anode) voltage. Furthermore, the correlation obtained from Figure 4.11 indicates that the average electron energy is between 2 and 9% lower than the potential applied at the anode.
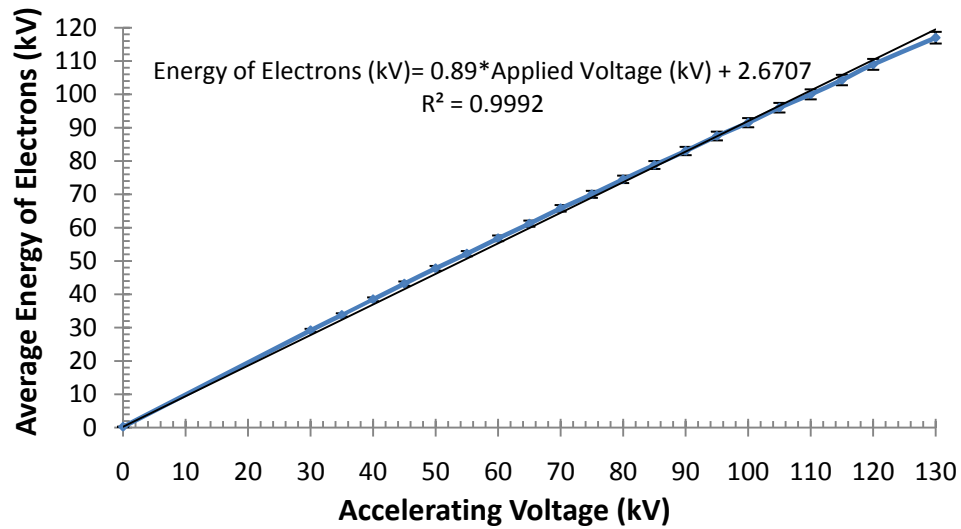
Figure 4.11. Average energy of electrons reaching the anode vs. anode (accelerating) voltage. The grid voltage for these simulations was kept at 45V.

4.5. ELECTRON DISTIBUTIONS AND FOCAL SPOT SIZES

As it was pointed out for Figure 4.10, determining the current density (mA/mm^2) and the energy distribution of electrons is not enough to completely characterize the beam of emitted electrons reaching the anode. In addition to these two quantities, it is necessary to consider the non-uniform distribution of electrons across the anode surface.

In this work, the energy distributions with and witout focusing were obtained for the 30 kV and 120 kV anode voltage cases. For each anode voltage case, the grid voltages considered in the simulations were 30, 40, 50 and 60V. The electrons distributions obtained from these simulations are summarized in Figure 4.12 and Figure 4.13 for the 30 kV and 120kV anode voltage cases respectively.
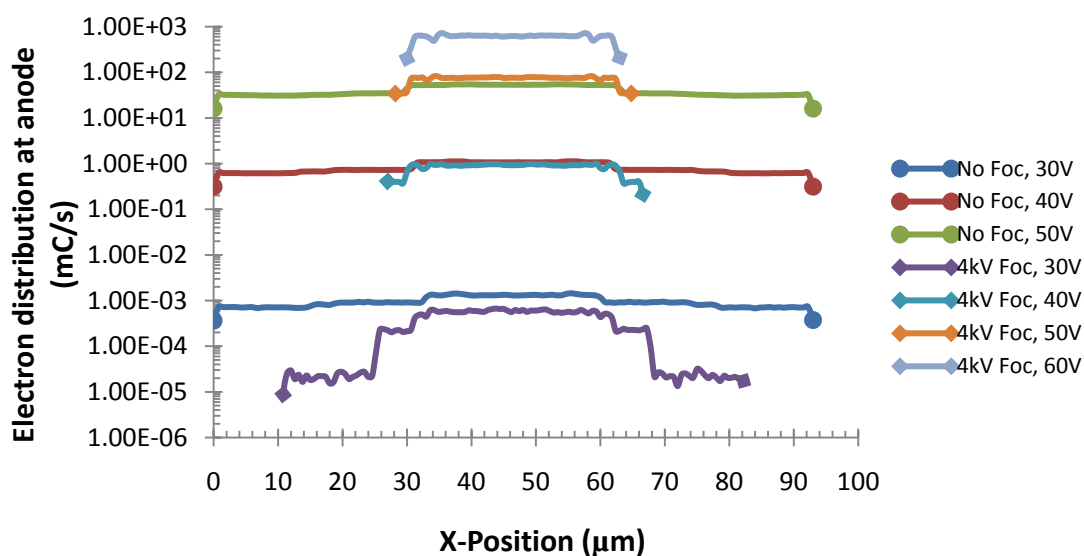
Figure 4.12. Electron distributions for the 30kV anode voltage case. Grid voltages: 30, 40, 50 and 60V, focusing voltage: 4kV.
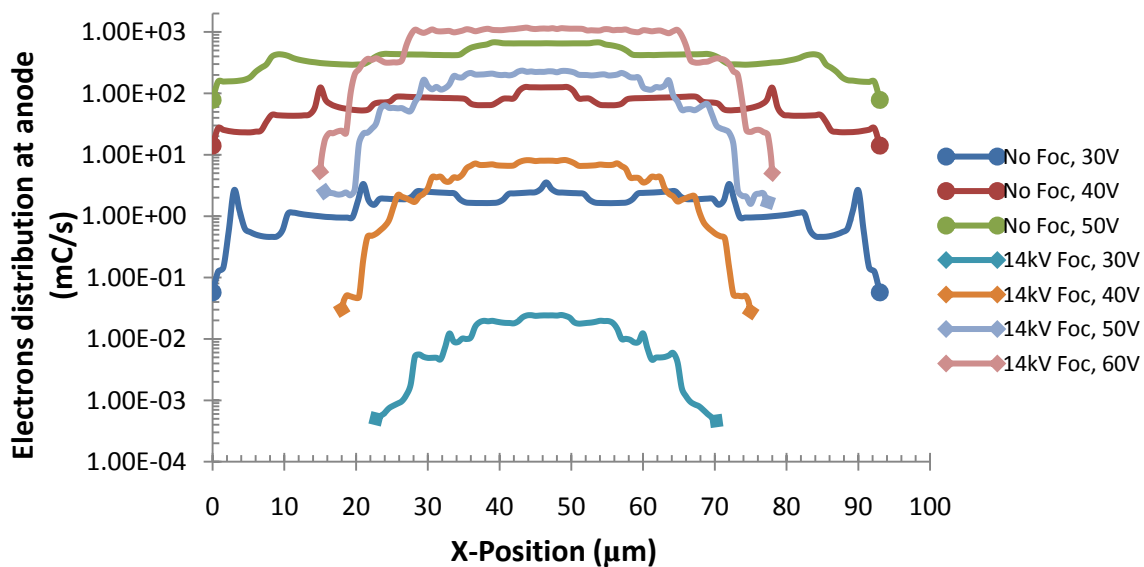
Figure 4.13. Electron distributions for the 120kV anode voltage case. Grid voltages: 30, 40, 50 and 60V, focusing voltage: 14kV.

A common trend found in Figure 4.12 and 4.13, it is the tendency of the number of electrons (mC/s) to be higher in the center of the triode structure. However, depending on both the voltage applied to the extraction grid and whether focusing structures are used several variations on the electron distributions are observed. Independently of the voltages applied at the anode, in cases where no focusing electrodes are included in the triode structure, electrons are distributed across the whole anode surface. In this case, the electron distribution was found to have a higher uniformity in the 30kV case compared to the 120kV case (see Figures 4.12 and 4.13). On the other hand, when focusing electrodes were included in the triode structure, the size of the spot where electrons strike the anode (*focal spot size*) was found to change with the voltage applied at the extraction grid. The relationship of the focal spot size with the grid voltage is shown in Figure 4.14. Results for the 30kV anode voltage case the focal spot size decreases as the extracting voltage increases, whereas for the 120kV case an increase in the focal spot size is observed as the voltage is increased. Using a typical triode structure, Chang et. al., [22] reported that for a 30kV anode voltage the focal spot size of the beam of electrons tend to decrease as the grid voltage is increased. Even though there are differences in the grid voltages applied and the geometries of the cells simulated, their results are in general agreement with the ones presented here.
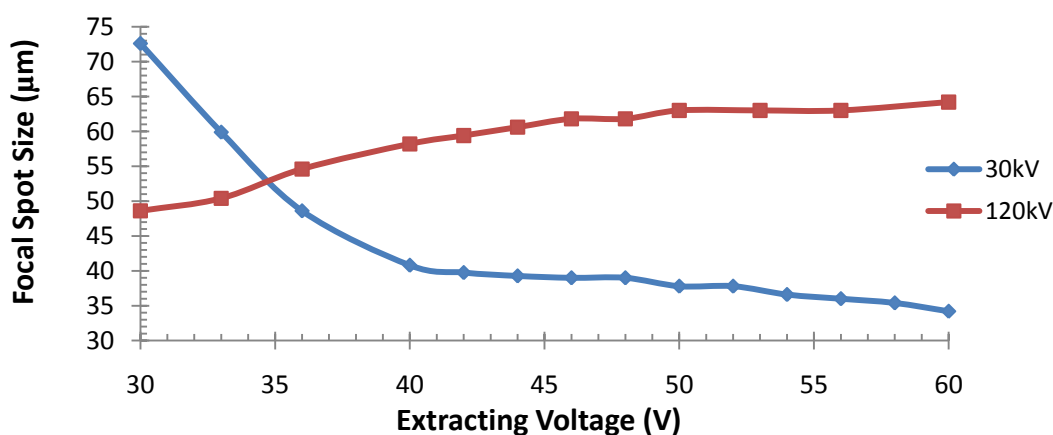
Figure 4.14. Focal spot size as a function of the extracting voltage. 30kV and 120kV anode voltage cases.

No previous results reporting the focal spot size of the electron beam in a triode structure operating at high anode voltages (>100kV) were found. This behavior the focal spot size at high anode voltages (>100kV) is believed to be associated with the difficulty in changing the original trajectory of the electrons due to their higher energies. For this reason, even though the electrons can be focused, they still tend to keep a proportion of their originally divergent trajectory. This effect is more evident as the extracting voltage is increased as it generates an increase in the number of emitted electrons. In addition, as the number of emitted electron increases, the effect of coulomb interactions will increase as well. However, results obtained from the simulations presented in this work do not permit to be conclusive about the tendency observed for the focal spot size in the 120kV case. In order to obtain a better understanding to this trend, more sophisticated 3-D simulations will be necessary and simulation results should be compared to experimental results.

4.6 ANODE CURRENT DENSITY VS. GRID APERTURE

In order to determine the effect on the current density, simulations were run for different grid apertures (see Figure 3.3 for details about grid configuration). As defined in Table 3.1, a grid aperture equal to 15 µm was used in all the simulations presented. In this case, additional simulations for the 30kV anode voltage case were run using grid apertures equal to 9, 12, and 18µm, results are presented in Figure 4.15.

At a given extracting voltage, the anode current density was found to increase as the grid aperture was increased as well. In comparison to the other grid aperture sizes simulated, the most significant difference was found for a grid aperture equal to 18 µm. This increase in the current density with the grid aperture is believed to be associated to a higher penetration of the high electric field generated in the grid-anode gap into the cathode-grid gap. As the grid aperture gets smaller, the effect of the high electric field on the emission current is reduced by the shielding effect observed around the grid in Figures 4.3 and 4.5.
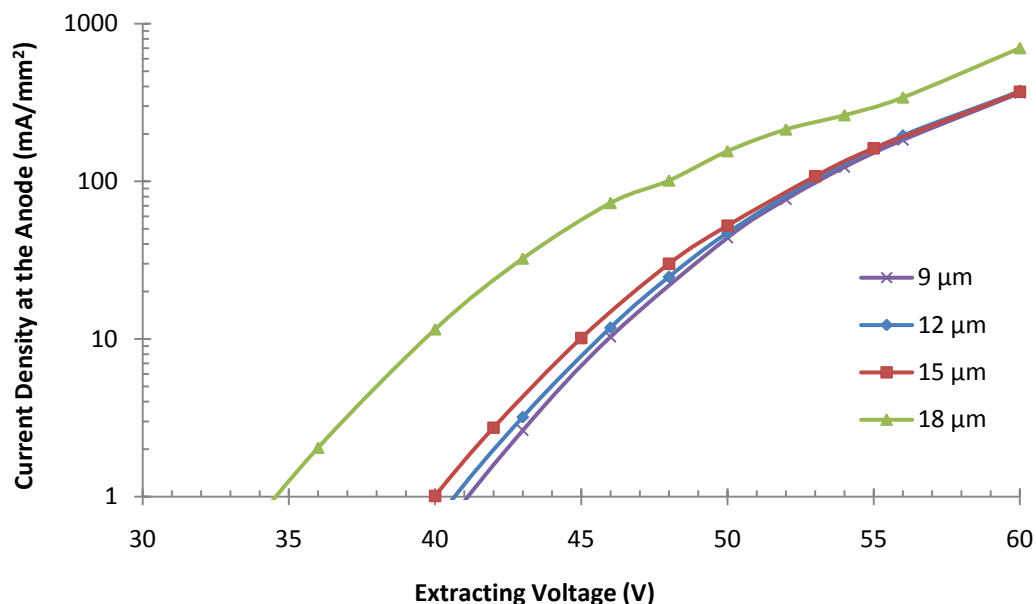
Figure 4.15. Anode current density (mA/mm^2) as a function of grid aperture. Anode voltage: 30kV.

As a consequence, at a given extracting voltage, current density values observed for smaller grid apertures were all close to each other, not showing significant differences.

In the 30kV anode voltage case, it was found that for an 18μm grid aperture, 1000μm was the minimum anode-cathode distance to be used before the emission of electrons due to the anode voltage would take place. For the same 30kV anode voltage case, when a grid aperture equal to 9μm was used, the minimum cathode-anode distance allowable before the emission of electrons due to the anode voltage occurred was as low as 200μm.

In the 120kV case, a grid aperture equal to 15μm was the minimum allowable before emission of electrons would occur due to the anode voltage. For the same anode voltage case, when the grid aperture size was reduced to 9μm, a cathode-anode distance as small as 300μm was found to be usable while preventing electrons to be emitted due to the anode voltage. These important results have yet to be verified experimentally, including testing for possible electric breakdown. However, if results here presented are proven to be an adequate physical representation of the simulated system, they can be

used to manipulate the grid aperture such that the anode-cathode distance in the triode structure can be minimized. In fact, due to the necessity of using microfabrication techniques, this minimization of the anode-cathode distance is expected to be a crucial issue during construction of a first prototype of the proposed flat panel x-ray source.

5. CONCLUSIONS

In this work, the field emission characteristics of a carbon nanotube based triode structure are simulated using the Particle in Cell code OOPIC Pro. The emission of electrons from the CNT-based cathode was simulated according to the Fowler-Nordheim field emission mechanism. Simulations were run for different grid and anode voltages and the effect of using focusing electrodes was analyzed as well.

The trajectory of electrons was found to be determined by the electric field lines established among the surfaces of the simulated structure. The beam of emitted electrons was found to have a divergent trajectory when no focusing electrodes were employed. This divergent trajectory was modified into a convergent one by adding focusing electrodes to the triode structure.

For the focused beam, the focal spot size was found to be influenced by the grid voltage. For the 30 kV anode voltage case, the focal spot size will decrease as the extracting voltage increases; the opposite behavior was observed at a higher anode voltage of 120 kV.

The J_{FN}-V curves constructed for the systems indicated that the electron current density is controlled via grid voltage. Although a small influence of the anode voltage on the electron current density was observed.

Space charge limitation phenomena were present in the simulated systems at high grid voltages. This space charge limitation phenomenon turned the continuous emission of electrons into an oscillatory one.

In general, simulations indicated the technical feasibility of the proposed Flat Panel X-ray Source. Experimental verification of the results presented in this document has not yet been done and is recommended for future work.

6. RECOMMENDATIONS FOR FUTURE WORK

Results obtained in this work indicated the technical feasibility of the CNTs-based triode structure to be used as source of electrons in each of the micro x-ray cells of the proposed distributed flat panel x-ray source. However, improvements in the Particle-in Cell model used to evaluate the field emission characteristics in the triode structure are still to be made. Consideration of additional geometries might improve the results obtained in the simulations. Also, further details such as secondary emission of electrons in the surfaces of the simulated structure, backscattering of high energy electrons from the anode surface, and gas ionization in the electron beam path should be considered in the PIC model in order to obtain more accurate results. However, it must be considered that the inclusion of further details in the OOPIC Pro model and the consideration of additional geometries is computationally expensive.

The characteristics of operation of the proposed x-ray source require the application of high voltage bias (as high as 120kV) between the small cathode-anode gap (~μm) under vacuum conditions. Due to the application of these high voltages in small gaps, the possibility of electrical breakdown in the system must be evaluated. Previous reports have been published indicating the possibility of using OOPIC Pro to evaluate the breakdown characteristics in systems.

Results presented in this thesis were all obtained considering that only DC voltages where applied in the triode structure. The consideration of a pulse-driven mode could provide an alternative to possible problems associated to the accumulation of charges in the walls of the triode structure. Also, this pulse-driven mode of the triode structure could be an alternative to possible breakdown problems.

Additionally, a comparison between simulations results and those obtained experimentally should be made. This comparison will provide valuable information to benchmark the proposed model and behavior characteristics of the proposed x-ray source.

APPENDIX

INPUT FILE USED FOR THE OOPIC PRO SIMULATIONS

Flat Panel X-ray- Field emission Calculations

{

This input file is used to determine the field emission characteristics

of a carbon-nanotube-based cathode located in a triode structure.

OOPIC PRO is the software used in the simulations.

The emitters are simulated according to the Fowler-Nordheim field

emission model implemented in OOPIC. This input file was adapted

from the Fowler_Nordheim.inp input file found in the OOPIC PRO libraries.

The model, which uses cartesian coordinates, corresponds to a triode structure,

composed of a cathode, an anode and an extraction grid. A DC potential difference

is generated across the lower boundary (cathode) and a medium boundary (extraction

grid)

in order to extract the electrons. A much higher DC potential is generated across

the cathode-anode gap in order to accelerate the electrons toward the anode.

Electrons are emitted from a portion of the lower boundary,

according to the Fowler-Nordheim field emission model.

Diagnostics of how much energy they have upon arrival upper boundary (anode)

is kept. Also, the energy, velocity, and distribution of the electrons striking the anode

are diagnosed.

An electrostatic field solver is used.

Modification V3 = All the grids are in place

Modification V4 = Central grids are removed

Modification V5 = Focusing electrodes where added

Modification V6 = Cell size is reduced (80 YCells) 1mm height for the cell

Modification V6-1= Trying to implement a pulse mode for the extracting voltage (rise_time effect)

Modification V6-2= Voltage diagnostics at the anode is added Modification V9= Rise time established as a variable of the simulation (initially set at 10 ps)

Modification V10= Focusing electrodes are added

}

Variables

{

```
//******************************************************************
//************** Geometrical Aspects of the Triode Structure **************
//******************************************************************
 //
 speedLight=2.99792458e+08
 //************** Geometrical Aspects of Ext_Grid *************************
    Gridthik= 0.000003              // Thickness of the metal wire in the extracting grid
    Gridspace= 0.000015             // Open space in the extracting grid
    Gridheight= 0.000001            // Height of the extracting Grid - "Thickness if you
// want to call it that way"
 //
 //************** Geometrical Aspects of Ext_Grid *************************
 //
  // ThickAnode= 0.00001            // Thickness of the Tungsten target
 //
//*******************************************************************
 //************** Geometrical Aspects of the Triode Structure **************
//*******************************************************************
  CellsX= (((6*Gridthik)+(5*Gridspace))*1000000)/3
 //CellsX=100
  numCellsX = CellsX              // # of cells along horizontal axis
```

xGridMKS = (6*Gridthik)+(5*Gridspace)   // Width of the grid

xMaxMKS = (6*Gridthik)+(5*Gridspace)   // Length of horizontal axis in meters

yMaxMKS = 0.001.

numCellsY = yMaxMKS*80000   // # of cells along vertical   axis

yGridMKS = 2   // Distance between emitters and extraction grid

                // Length of vertical   axis in meters

//xDivisions= 51   // # of divisions defined for the extraction grid

                                // (For the sake of symmetry, it has to be a odd number)

numEmitterCells = 0.5*numCellsX   // # of cells along the emitting surface.

                                // This number increases the area of the emitter

Grid_thik= Gridthik*1000000/3

Grid_space= Gridspace*1000000/3

Grid_height= Gridheight*1000000/1

dx=xMaxMKS/numCellsX

dy=yMaxMKS/numCellsY

d=1./sqrt(1./(dx*dx)+1./(dy*dy))

//timeStep=0.05*d/speedLight

yGrid=yMaxMKS/numCellsY

timeStep=0.5*yGrid/speedLight

risetime=10e-12   // Rise Time of Extracting Voltage

//

// ***

// *************** Potentials Applied to the Triode Structure ****************

// ***

//

npart=1e+05   // numerical weight of emitted particles

AnodePotential= 31000   // Accelerating voltage @ the anode (V) (positive   // for

electrons to be attracted

GridPotential= 50//105   // Potential Specified @ extracting grid (V)

// (negative for electrons to be emitted)

CathodePot= 0 // Potential Specified at the emitting cathode (Must // be negative respect

to GridPotential)

ElecPotential= 4000   // Potential specified for the focusing lens (positive

//- electrons to be repeled)

 //

//**

 //*************** Potentials Applied to the Triode Structure ****************

//**

   }

//

//

//**

//******* Definition of Geometry, Max and Min Coordinates in the Grid *********

//**

  Region

  {

  Grid

  {

  J   = numCellsX   // number of grids in x

  x1s = 0.0   // Lower coordinate in x1

  x1f = xMaxMKS   // Upper coordinate in x1

  n1=1.0

  K   = numCellsY   // number of grids in y

  x2s = 0.0   // Lower coordinate in y

```
    x2f = yMaxMKS              // Upper coordinate in y
    n2=1.0


  Geometry = 1                 // 0 to specify Cylindrical Geometry
                               // 1 to specify Cartesian Geometry
   }
//
//**********************************************************************
//******* Definition of Geometry, Max and Min Coordinates in the Grid *********
//**********************************************************************
//
//
//**********************************************************************
//*************** Creation and Definition of Species *********************
//**************** to be used along the simulation  *********************
//**********************************************************************
//
  Species
   {
    name = electrons               // name is used below for emitter
    m = 9.11E-31                   // electron mass in KG
    q = -1.6e-19                   // electron charge in C
    rmsDiagnosticsFlag=1           // Collect time history plots on RMS values for
                                   // beam size and velocity
    collisionModel=electron        // Model to simulate collisions of electrons
   }
//
//**********************************************************************
//*************** Creation and Definition of Species *********************
//**************** to be used along the simulation  *********************
//**********************************************************************
```

Control

  {

  dt = timeStep   // the time step in s

  ElectrostaticFlag = 1   // specify use of the electrostatic field solve

  }

//

// The top boundary is a perfect conductor.

// It is further specified that some energy diagnostics should be collected

//   for particles that strike this boundary.

//

//***

//*********************** Begining Extrac_Grid ***********************

//***

//

//***

//*************** Bottom-Sides of the grid ****************************

//***

Equipotential

{

name=Extract_grid

// Segments for grid #1 (Counting from left to right)

Segment //Bottom boundary

{

 j1 = 0

 j2 = Grid_thik

 k1 = yGridMKS

 k2 = yGridMKS

 normal = -1

}

Segment // top boundary

{

```
 j1 = 0
 j2 = Grid_thik
 k1 = yGridMKS+Grid_height
 k2 = yGridMKS+Grid_height
 normal = 1
}
Segment // left Boundary
{
 j1 = 0
 j2 = 0
 k1 = yGridMKS
 k2 = yGridMKS+Grid_height
 normal = 1
}
Segment // right boundary
{
 j1 = Grid_thik
 j2 = Grid_thik
 k1 = yGridMKS
 k2 = yGridMKS+Grid_height
 normal = 1
}


// Segments for grid #2 (Counting from left to right)
Segment // Bottom boundary
{
 j1 = (Grid_thik)+(1*Grid_space)
 j2 = (2*Grid_thik)+(1*Grid_space)
 k1 = yGridMKS
 k2 = yGridMKS
 normal = -1
```

```
}
Segment // Top boundary
{
 j1 = (Grid_thik)+(1*Grid_space)
 j2 = (2*Grid_thik)+(1*Grid_space)
 k1 = yGridMKS+Grid_height
 k2 = yGridMKS+Grid_height
 normal = 1
}
Segment // Left boundary
{
 j1 = (Grid_thik)+(1*Grid_space)
 j2 = (Grid_thik)+(1*Grid_space)
 k1 = yGridMKS
 k2 = yGridMKS+Grid_height
 normal = -1
}
Segment // Right boundary
{
 j1 = (2*Grid_thik)+(1*Grid_space)
 j2 = (2*Grid_thik)+(1*Grid_space)
 k1 = yGridMKS
 k2 = yGridMKS+Grid_height
 normal = 1
}

// Segments for grid #3 (Counting from left to right)
Segment // Bottom boundary
{
 j1 = (2*Grid_thik)+(2*Grid_space)
 j2 = (3*Grid_thik)+(2*Grid_space)
```

```
 k1 = yGridMKS
 k2 = yGridMKS
 normal = -1
}
Segment // Top boundary
{
 j1 = (2*Grid_thik)+(2*Grid_space)
 j2 = (3*Grid_thik)+(2*Grid_space)
 k1 = yGridMKS+Grid_height
 k2 = yGridMKS+Grid_height
 normal = 1
}
Segment // Left Boundary
{
 j1 = (2*Grid_thik)+(2*Grid_space)
 j2 = (2*Grid_thik)+(2*Grid_space)
 k1 = yGridMKS
 k2 = yGridMKS+Grid_height
 normal = -1
}
Segment // Right Boundary
{
 j1 = (3*Grid_thik)+(2*Grid_space)
 j2 = (3*Grid_thik)+(2*Grid_space)
 k1 = yGridMKS
 k2 = yGridMKS+Grid_height
 normal = 1
}


// Segments for grid #4 (Counting from left to right)
Segment // Bottom Boundary
```

```
{
 j1 = (3*Grid_thik)+(3*Grid_space)
 j2 = (4*Grid_thik)+(3*Grid_space)
 k1 = yGridMKS
 k2 = yGridMKS
 normal = -1
}
Segment // Top boundary
{
 j1 = (3*Grid_thik)+(3*Grid_space)
 j2 = (4*Grid_thik)+(3*Grid_space)
 k1 = yGridMKS+Grid_height
 k2 = yGridMKS+Grid_height
 normal = 1
}
Segment  // Left Boundary
{
 j1 = (3*Grid_thik)+(3*Grid_space)
 j2 = (3*Grid_thik)+(3*Grid_space)
 k1 = yGridMKS
 k2 = yGridMKS+Grid_height
 normal = -1
}
Segment // Right boundary
{
 j1 = (4*Grid_thik)+(3*Grid_space)
 j2 = (4*Grid_thik)+(3*Grid_space)
 k1 = yGridMKS
 k2 = yGridMKS+Grid_height
 normal = 1
}
```

```
// Segments for grid #5 (Counting from left to right)
Segment // Bottom boundary
{
 j1 = (4*Grid_thik)+(4*Grid_space)
 j2 = (5*Grid_thik)+(4*Grid_space)
 k1 = yGridMKS
 k2 = yGridMKS
 normal = -1
}
Segment // Top Boundary
{
 j1 = (4*Grid_thik)+(4*Grid_space)
 j2 = (5*Grid_thik)+(4*Grid_space)
 k1 = yGridMKS+Grid_height
 k2 = yGridMKS+Grid_height
 normal = 1
}
Segment  // Left Boundary
{
 j1 = (4*Grid_thik)+(4*Grid_space)
 j2 = (4*Grid_thik)+(4*Grid_space)
 k1 = yGridMKS
 k2 = yGridMKS+Grid_height
 normal = -1
}
Segment // Right Boundary
{
 j1 = (5*Grid_thik)+(4*Grid_space)
 j2 = (5*Grid_thik)+(4*Grid_space)
 k1 = yGridMKS
```

```
  k2 = yGridMKS+Grid_height

  normal = 1

}


// Segments for grid #6 (Counting from left to right)
Segment // Bottom Boundary
{
  j1 = (5*Grid_thik)+(5*Grid_space)
  j2 = (6*Grid_thik)+(5*Grid_space)
  k1 = yGridMKS
  k2 = yGridMKS
  normal = -1
}
Segment // Top boundary
{
  j1 = (5*Grid_thik)+(5*Grid_space)
  j2 = (6*Grid_thik)+(5*Grid_space)
  k1 = yGridMKS+Grid_height
  k2 = yGridMKS+Grid_height
  normal = 1
}
Segment // Left Boundary
{
  j1 = (5*Grid_thik)+(5*Grid_space)
  j2 = (5*Grid_thik)+(5*Grid_space)
  k1 = yGridMKS
  k2 = yGridMKS+Grid_height
  normal = -1
}
Segment // Right Boundary
{
```

```
 j1 = (6*Grid_thik)+(5*Grid_space)
 j2 = (6*Grid_thik)+(5*Grid_space)
 k1 = yGridMKS
 k2 = yGridMKS+Grid_height
 normal = 1
}


  xtFlag=0   // Tells OOPIC to take F as the voltage function instead of using A or C
//fill=1    // It implies the boundary is closed


// IdiagFlag = 1           // TData accumulator for particle current


 //tdelay = 2E-12
 //trise = 2E-15
 //tpulse = 2E-8
 //tfall = 2E-12
 //a0 = 1
 //a1 = 2


 // F = 2*step(sin((2*3.14/2E-11)*t + 90)) // Square Pulses


 // F=-100*pulse(t,2E-12,2E-12,2E-12,2E-12) - 100*pulse(t,10E-12,2E-12,2E-12,2E-
12)-5*pulse(t,20E-12,2E-12,2E-12,2E-12)
    a0 = 0
    a1 = 1
    C = GridPotential            // Voltage applied to the extraction grid
    trise = risetime


 //nxbins = 2.*numCellsX      // resolution of position diagnostic
 // number of spatial bins along boundary segment for Dist. Accumulation)
```

```
// nenergybins = 40          // resolution of the energy diagnostic
// energy_min  = 0           // in eV
// energy_max  = 30000       // in eV
 }


//*********************************************************************
//******************** Top Sides of the Grid **************************
//*********************************************************************
//
//*********************************************************************
//************************** Polarizer ********************************
//*********************************************************************
//Polarizer
//{
//  name=polarizer
//  j1 = 0
 //  j2 = numCellsX
//  k1 = yGridMKS
//  k2 = yGridMKS
//  normal=1
//  transmissivity=1


//  IdiagFlag = 1          // TData accumulator for particle current


//  Ihist_avg=10            // (int) Number of timesteps for averaging current plots.
//  Ihist_len=1024           // (int) Length of the current history arrays.
// diagSpeciesName= electrons    // (string) species for distribution function
// accumulation. If not present or set to "Noname", the diagnostic is off.
//  nxbins=100               // (int) Number of spatial bins along boundary segment for
                    // accumulation.
//  nenergybins = 40         // resolution of the energy diagnostic
```

```
//   energy_min  = 0       // in eV
 //  energy_max  = 30000         // in eV


//}
//********************************************************************
//**************** Right Side of the Grid *****************************
//********************************************************************
//*********************** End Extracting Grid ************************
//********************************************************************
//
//********************************************************************
//*********************** Beginning Cathode **************************
//********************************************************************
//
// The bottom boundary is an equipotential surface.

Equipotential
{
  name=cathode
   j1 = 0
   j2 = numCellsX
   k1 = 0
   k2 = 0
   normal=1

   C = CathodePot                // specified potential in V (negative respect to GridPot for
// electrons to be emitted)
 }
//
//********************************************************************
//*********************** End Cathode********************************
```

```
//*********************************************************************
//
//*********************************************************************
//********************* F-N Emitter*********************************
//*********************************************************************
//
// In the following lines, a portion (50%) of the bottom boundary surface is specified
// to be a surface that emits electrons via the Fowler-Nordheim field
// emission model.
//
//  Below, there are specificied the  Fowler-Nordheim parameters reported in the literature
//  for carbon nanotubes. Some of them are given their default value though
//
FowlerNordheimEmitter
{
   // Bottom side of the emitter of five microns hight
      j1 = ((numCellsX - numEmitterCells) / 2)        // Initial Possition of the emitter in X
      j2 = (numCellsX + numEmitterCells) / 2          // Final Possition of the emitter in X
      k1 = 0
      k2 = 0
      normal=1
 //
 //
 //
      speciesName = electrons                    // name from species group above
      np2c = npart                               // numerical weight of emitted particles
 //
 // Coefficient "A" of the Fowler-Nordheim field emission model.
      A_FN = 1.5414e-06       // The default value is 1.5414e-06, which is specified here.
 //
 // Coefficient "beta" of the Fowler-Nordheim field emission model.
```

```
        beta_FN = 2200.        // Field enhancement of the material.
// The default value is 1.  Here, we specify beta_FN = 2200, which corresponds to // a
accepted value for Carbon nanotubes


 //
     B_FN = 6.8308e+09     // Coefficient "B" of the Fowler-Nordheim FE model.
                            // The default value is 6.8308e+09, which is specified here.
 //
 //
     C_v_FN = 0.      // Coefficient "C_v" of the Fowler-Nordheim field emission model.
                        // The default value is 0, which is specified here.
 //
 //
     C_y_FN = 3.79e-05      // Coefficient "C_y" of the Fowler-Nordheim FE model.
                            // The default value is 3.79e-05, which is specified here.
 //
 //
     Phi_w_FN = 5.0.// The work function "Phi_w" for electrons in the surface, in eV.
                      // value 0f 5 eV taken as representative for CNTs samples.
 //
                        // The number of intervals to be used for emitting particles.
     nIntervals = 0     // The default value of 0, which is specified here.
                        // In the default case, nIntervals will be reset to the # of cells
                        // along the emitting boundary (with a minimum of 2), which  is
                        // the most reasonable thing to do.
 //
 //      fill=1                        // it implies the boundary is closed


 }
```

```
//*************************************************************
//******************* Begining of the Anode *********************
//*************************************************************
Equipotential
{
 name = anode
// Top side of the anode
   j1 = 0
   j2 = numCellsX
   k1 = numCellsY
   k2 = numCellsY
   normal = -1                        // Unit direction of the face normal. (-1):Down/Left


   C = AnodePotential          // Specified potential in V (+  for e- to be attracted)


// In the following code lines it is specified the energy diagnostics to be collected
// for particles that strike on this boundary.


 IdiagFlag = 1              // TData accumulator for particle current
 Ihist_avg=100             // (int) Number of timesteps for averaging current plots.
 Ihist_len=1024            // (int) Length of the current history arrays.
 nxbins = 5.*numCellsX     // resolution of position diagnostic
// number of spatial bins along boundary segment for Dist. Accumulation)
 nenergybins = 5.*numCellsX      // resolution of the energy diagnostic
 energy_min  = 0               // in eV
 energy_max  = 31000           // in eV
 }
```

```
//*************************************************************
//********************** Side boundaries *********************
//*************************************************************
// The left boundary is a simple dielectric
Dielectric
{
  j1 = 0
  j2 = 0
  k1 = 0
  k2 = numCellsY
  normal=1
}
// The right boundary is a simple dielectric
Dielectric
{
  j1 = numCellsX
  j2 = numCellsX
  k1 = 0
  k2 = numCellsY
  normal = -1
}
//*************************************************************
//********************** Side boundaries *********************
//*************************************************************
//*************************************************************
//
//************************* Begining *************************
//********************* Initial density of electrons ***************
//*************************************************************

//Load
```

```
//{
//      units=EV
//      x1MinMKS = 0
//      x1MaxMKS = 0.00015
//      x2MinMKS = 0.000070
//      x2MaxMKS = 0.001
//      speciesName = electrons
//      density = 1.0e15
//      np2c = 1.0e6
//      LoadMethodFlag =0
//      temperature = 0
//}


//*************************************************************
//*********************** End ********************************
//********************* Initial density of electrons **************
//*************************************************************

Diagnostic
{
  j1 = 0
  j2 = numCellsX
  k1 = numCellsY-1
  k2 = numCellsY-1
  title = Anode Voltage
  VarName = phi
  HistMax = 1024
  Comb = 2
  x1_Label=X
  x2_Label=Time
  x3_Label=Potential
```

```
}


//*************************************************************
//******************* Focusing lens **************************
//*************************************************************
Equipotential
{
name=Foc_left // left focusing Electrode.
Segment // Right side
{
 j1 = 1
 j2 = 1
 k1 = 25
 k2 = 27
 normal=1
}
Segment // Left side
{
 j1 = 0
 j2 = 0
 k1 = 25
 k2 = 27
 normal=1


}
Segment// Up side
{
 j1 = 0
 j2 = 1
 k1 = 27
 k2 = 27
```

```
   normal=1


}
Segment // Bottom side
{
 j1 = 0
 j2 = 1
 k1 = 25
 k2 = 25
 normal=-1


}
 C=ElecPotential
}


Equipotential
{
name=Foc_Right // Focusing lens...Right side
Segment // Right side
{
 j1 = numCellsX
 j2 = numCellsX
 k1 = 25
 k2 = 27
 normal=-1
}
Segment // Left side
{
 j1 = numCellsX-1
 j2 = numCellsX-1
 k1 = 25
```

```
  k2 = 27
  normal=-1


}
Segment// Up side
{
 j1 = numCellsX-1
 j2 = numCellsX
 k1 = 27
 k2 = 27
 normal=1


}
Segment // Bottom side
{
 j1 = numCellsX-1
 j2 = numCellsX
 k1 = 25
 k2 = 25
 normal=-1


}
 C=ElecPotential
}
//************* Final bracket ***********
}
```

BIBLIOGRAPHY

[1] A. Worlbarst, [*Physics of Radiology*] Medical Physics Publishing. Madison, WI. (2005).

[2] R. H. Fowler, and L. Nordheim, *"Electron emission in Intense Electric Fields,"* Proc. R. Soc. Lond. A, 119, pp. 173-181 (1928).

[3] R. C. Smith and S.R.P. Silva, *"Design of carbon nanotubes for large-area electron field-emission cathodes,"* Journal of the SID, 16, pp. 615-624 (2008).

[4] Z. B. Li, S.Z., Deng and N.S., Xu, *"Mechanism of field electron emission from carbon nanotubes,"* Front. Phys., 3, 305 (2006).

[5] S. Chhoker, S. K. Srivastava and V.D. Vankar, *"Field emission properties of carbon nanostructures: A review,"* Int. Work. on Phys. Semi. Dev, 2007. IWPSD, 16-20 Dec. 2007 pp. 820-826.

[6] J. B. Hudson, [Surface Sciende: An Introduction] John Wiley & Sons, Inc. Troy, NY. 27-48 (1998).

[7] C. H., Castano, *"Study of breakdown/arcing for high power RF antennas on fusion applications,"* Ph.D. Dissertation, Chapter 3, University of Illinois at Urbana-Champaign (2006).

[8] R. Bacon, *"Growth, Structure, and Properties of Graphite Whiskers"* Journal of Applied Physics,31, 284-290 (1960).

[9] S. Iijima, *"Helical microtubules of graphitic carbon,"* Nature, 354, pp. 56-58 (1991)

[10] G.E. Ioannatos and X. E. Verykios, *"H^2 storage on single- and multi-walled carbon nanotubes,"* International Journal of Hydrogen Energy, 35, 622-628 (2010).

[11] W. Hoenlein, F. Kreupl, G.S. Duesberg, A.P. Graham, M. Liebau, R. Seidel and E. Unger, *"Carbon nanotubes for microelectronics: status and future prospects,"* Materials Science and Engineering C, 23, 663-669 (2003).

[12] A.M.K. Esawi and M.M. Farag, *"Carbon nanotube reinforced composites: Potential and current challenges,"* Materials and Design, 28, 2394-2401 (2009).

[13] L. Chunyu, T. E. Thostenson and T. W. Chou, *"Sensors and actuators based on carbon nanotubes and their composites: A review,"* Composites Science and Technology, 68, 1227-1249 (2008).

[14] E. Frackowiak and F. Beguin, *"Carbon materials for the electrochemical storage of energy in capacitors,"* Carbon, 39, 937-950 (2001).

[15] M. Nakamoto, *"Current Trends in Field Emission Displays,"* Proc. I4, 978, (2008).

[16] R.H. Baughman, A.A. Zakhidov and W. A. de Heer, *"Carbon Nanotubes: The Route toward Applications,"* Science, New Series, 297, 787-792 (2002).

[17] W. A. de Heer, A. Chatelain and D. Ugarte, *"A Carbon Nanotube Field-Emission Electron Source,"* Science, New Series, 270, 1179-1180 (1995).

[18] http://20.nas.nasa.gov/Groups/SciTech/nano/images/roll_graphite.gif. Cited: 01/16/2011

[19] N. de Jonge and J.M. Bonard, *"Carbon nanotubes electron sources and applications,"* Phil. Trans. R. Soc. Lond. A, 362, 2239-2266 (2004).

[20] A. V. Eletskii, and G.S. Bocharov, *"Emission properties of carbon nanotubes and cathodes on their basis,"* Plasma Sources Sci. Technol., 18, (2009).

[21] J. Janik, F. Balon, P. Viduska and T. Danis *"Field and electron trajectory modeling in the vicinity of an emitting tip,"* J. Vac. Sci. Technol. B 24(4), 1951-1955, (2006).

[22] W.S. Chang, H.Y. Choi and J.U. Kim, *"Simulation of Field-Emission Triode Using Carbon Nanotube Emitters,"* Japanese Journal of Applied Physics 45, pp.7175-7180 (2006).

[23] H.Y. Choi and J. U. KIM, *"Carbon-Nanotube (CNT)-Based Triode X-ray Tube Design by Using Computer Simulation,"* J. Korean Physical Society, 53, 1388-1392 (2008).

[24] Y. Di, W. Lei, X. Zhang, Y. Cui and Q. Wang, *"A new Triode Structure With a Carbon Nanotube Cathode,"* I4 Transactions on Electron Devices, 54, 3079-3084 (2007).

[25] A.L. Musatov, Y.V. Gulyaev, K.R. Izraek'yants, E.F. Kukovitskii, N.A. Kiselev, O.Y. Maslennikov, I.A. Guzilov, A.B. Ormont, and E.G. Chirkova, *"A compact X-ray Tube with a Field Emitter Based on Carbon Nanotubes,"* Journal of Communications Technology and Electronics, 52, 714-716 (2007).

[26] Y. Cheng and O. Zhou, *"Electron field emission from carbon nanotubes,"* C. R. Physique, 4, 1021-1033 (2003).

[27] T.S. Kim, Y.J. An, K.H. Kim, W.S. Chung and Y.R. Cho, *"Simulations of the Dielectric Cconstant of Bonding Materials and Field Emission Properties of CNTs Cathodes,"* Metals and Materials International, 12, 339-343 (2006).

[28] E.J. Grant, C.M. Posada, C.H. Castano and H.K. Lee, *"Electron field emission particle in cell (PIC) coupled with MCNPX simulation of a CNT-based flat-panel-x-ray source,"* Proc. of SPIE, 7961-7 (2011) In Press.

[29] J.P. Verboncoeur, A.B. Langdon and N.T. Gladd, *"An object-oriented electromagnetic PIC code,"* Computer Physics Communications, 87, 199-211 (1995).

[30] OOPOC Pro User's Guide, Version 2.0.2. Tech-X Corporation. http://20.txcorp.com/pdf/OOPIC_Pro/documentation/OOPIC_Pro_UsersGuide.pdf Cited: 02/22/2011

[31] D.M. Garner, *"Modelling of Emitted Current Distribution and Electron Trajectories in the Thin-Film Field-Emission Triode,"* Journal of Vacuum Science Technology B 22, pp. 1250-1256 (2004).

[32] J. Zhang, G. Yang, Y. Cheng, B. Gao, Q. Qiu, Y.Z. Lee, J.P. Lu and O. Zhou, *"Stationary scanning x-ray source based on carbon nanotubes field emitters,"* Applied physics letters, 86, 184104 (2005).

[33] J.W. Lugisland, Y.Y. Lau, and R.M. Gilgenbach, *"Two-Dimensional Child-Langmuir Law"* Physical Review Letters 77, pp. 4668-4670 (1996).

[34] H.Y. Choi, W.S. Chang, H.S. Kim, Y.H. Park and J.U. Kim, *"Acquisition of X-ray images by using a CNT cold emitter,"* Physics Letters A 357, pp. 36-41 (2006).

[35] R.G. Forbes and J.H.B Deane, *"Reformulation of the standard theory of Fowler-Nordheim tunneling and cold field electron emission"* Proc. R. Soc. A 463, pp. 2907-2927 (2007).

VITA

Chrystian Mauricio Posada Arbeláez was born in Amalfi, Antioquia, Colombia on August 24, 1986. He received his Bachelor of Science degree in chemical engineering from the Universidad Nacional de Colombia, sede Medellín – National University of Colombia – in March 2008. Being part of the research group on alternative fuels at the National University of Colombia, Chrystian developed his undergraduate thesis: "Determination of the optimum conditions for the transesterification reaction of castor bean oil for biodiesel production". After receiving his degree in chemical engineering, Chrystian worked in Medellin, Colombia for a multinational food company for almost a year.

Chrystian is currently a member of the American Nuclear Society and the Alpha Nu Sigma Honor Society. In January 2009 Chrystian began his studies at the Missouri University of Science and Technology and earned the Master of Science degree in Nuclear Engineering in May, 2011.